International Journal of Plasticity 108 (2018) 144–168

Contents lists available at ScienceDirect

International Journal of Plasticity

journal homepage: www.elsevier.com/locate/ijplas

Mechanical response of stainless steel subjected to biaxial load path changes: Cruciform experiments and multi-scale modeling

Manas V. Upadhyay[a], Anirban Patra[b,1], Wei Wen[b], Tobias Panzner[c], Steven Van Petegem[a], Carlos N. Tomé[b], Ricardo A. Lebensohn[b], Helena Van Swygenhoven[a,d,*]

[a] Photons for Engineering and Manufacturing Group, Laboratory for Synchrotron Radiation - Condensed Matter, Photon Science Division, Paul Scherrer Institute, CH-5232 Villigen PSI, Switzerland
[b] MST-8, Theoretical Division, Los Alamos National Laboratory, Los Alamos, NM 87545, USA
[c] Neutrons for Imaging and Activation Group, Laboratory for Neutron Scattering, Neutrons and Muons Division, Paul Scherrer Institute, CH-5232 Villigen PSI, Switzerland
[d] Neutrons and X-rays for Mechanics of Materials, IMX, Ecole Polytechnique Federale de Lausanne, CH-1012 Lausanne, Switzerland

ARTICLE INFO

Keywords:
Bauschinger effect
C mechanical testing
C finite elements
B crystal plasticity
A microstructures

ABSTRACT

We propose a multi-scale modeling approach that can simulate the microstructural and mechanical behavior of metal/alloy parts with complex geometries subjected to multi-axial load path changes. The model is used to understand the biaxial load path change behavior of 316L stainless steel cruciform samples. At the macroscale, a finite element approach is used to simulate the cruciform geometry and numerically predict the gauge stresses, which are difficult to obtain analytically. At each material point in the finite element mesh, the anisotropic viscoplastic self-consistent model is used to simulate the role of texture evolution on the mechanical response. At the single crystal level, a dislocation density based hardening law that appropriately captures the role of multi-axial load path changes on slip activity is used. The combined approach is experimentally validated using cruciform samples subjected to uniaxial load and unload followed by different biaxial reloads in the angular range [27°, 90°]. Polycrystalline yield surfaces before and after load path changes are generated using the full-field elasto-viscoplastic fast Fourier transform model to study the influence of the deformation history and reloading direction on the mechanical response, including the Bauschinger effect, of these cruciform samples. Results reveal that the Bauschinger effect is strongly dependent on the first loading direction and strain, intergranular and macroscopic residual stresses after first load, and the reloading angle. The microstructural origins of the mechanical response are discussed.

1. Introduction

1.1. Background and motivation

Engineering metals and alloys are often subjected to multi-axial load path changes during their fabrication (to form them into the

* Corresponding author. Photons for Engineering and Manufacturing Group, Laboratory for Synchrotron Radiation - Condensed Matter, Photon Science Division, Paul Scherrer Institute, CH-5232 Villigen PSI, Switzerland.
E-mail address: helena.vanswygenhoven@psi.ch (H. Van Swygenhoven).
[1] Current address: Department of Metallurgical Engineering and Materials Science, Indian Institute of Technology Bombay, Powai – 400076, India.

https://doi.org/10.1016/j.ijplas.2018.05.003
Received 2 November 2017; Received in revised form 4 May 2018; Accepted 5 May 2018
Available online 08 May 2018

desired shape) or under service conditions. The subsequent mechanical response of these materials significantly depends on their deformation history. For instance, a load reversal after a uniaxial tension, compression or shear can result in lowering the yield stress i.e. the Bauschinger effect, an extended elastic-plastic transition regime and a different hardening regime. The origin of such macroscopic behavior has to be found in the microstructural response. At the meso-scale or intergranular level, crystallographic texture evolution and anisotropy play a major role, and at the microscale or intra-granular level, heterogeneous dislocation activity combined with latent hardening effects have to be taken into account (Beyerlein and Tomé, 2007; Christodoulou et al., 1986; Rauch et al., 2007; Takahashi and Shiono, 1991).

Significant experimental and simulation efforts have been dedicated to understand the mechanical behavior of materials after a 180° load path change from uniaxial tension, compression or shear, at different strain levels and strain rates; a few recent examples are (Borodachenkova et al., 2015; Ha et al., 2017; Wang et al., 2014; Weiss et al., 2015). During forming processes or under service conditions, materials are often subjected to load path changes at reloading angles other than 180°. However, load path changes other than load reversals have received relatively much less attention; a few examples are recalled here. A combined in-situ neutron diffraction and crystal plasticity approach was used to study the macroscopic and microscopic response of 316L austenitic stainless steel dog-bone samples subjected to different combinations of 90° strain path changes (Gonzalez et al., 2012). In another work, rolled and uniaxially compressed commercially pure aluminum AA1050 was subjected to uniaxial tension along transverse and longitudinal directions (Mánik et al., 2015). Liao and co-workers (Liao et al., 2017) cut sub-sized dog-bones at 0°, 45° and 90° angles relative to the first monotonic tensile loading direction and compared their microstructural changes under uniaxial tensile reloading. Lee and co-workers (Lee et al., 2016) used cruciform sample geometries to study equibiaxial loading, unloading and reloading paths in advanced high strength steels. These studies concur that the first loading direction, accumulated strain, residual stresses, texture, elastic/plastic anisotropy, dislocation activity and reloading direction affect the subsequent macroscopic yield response and work-hardening behavior. Therefore, a thorough understanding of the load path change behavior of a material requires accounting for these effects.

Amongst all the aforementioned mechanical testing approaches, cruciform testing is the most versatile method to study non-proportional biaxial load path changes. The cruciform geometry allows the possibility to apply any arbitrary biaxial load, thus providing access to a large portion of the 2-dimensional stress/strain space; additionally, load path changes can be performed along any in-plane reloading direction without interruption. In spite of these advantages, cruciform samples have mainly been used for monotonic biaxial loading studies (see (Kuwabara, 2007; Upadhyay et al., 2017b) and the references within); applications to study the role of biaxial load path changes on the macroscopic response (Kuwabara et al., 2000; Merklein et al., 2014), and more recently, on the microstructural response (Collins et al., 2015, 2017; Van Petegem et al., 2016) are limited. This is mainly because it is difficult to determine the cruciform gauge stresses analytically. Furthermore, in some cruciform geometries, the in-plane gauge stresses are coupled with the applied load along both directions (Upadhyay et al., 2017b). This coupling is linear in the elastic regime (Bonnand et al., 2011; Cláudio et al., 2014; Hoferlin et al., 1998) with the in-plane (say directions 1 and 2) macroscopic stress components (Σ_{11}, Σ_{22}) related to the applied forces in the arms (F_1, F_2) as $\Sigma_{11} = aF_1 + bF_2$ and $\Sigma_{22} = bF_1 + aF_2$; where a and b are constant measures of cross-sectional area in the elastic regime. Defining the magnitudes of a and b is not trivial for most cruciform geometries, making it difficult to compute the gauge stresses analytically. Furthermore, a and b evolve non-linearly in the plastic regime resulting in a non-linear force-stress coupling. This makes it even more difficult to follow the gauge stress evolution, and consequently the yield and hardening behavior. Most cruciform designs, except those based on the ISO standard for biaxial testing (Deng et al., 2015; Kuwabara et al., 1998; Kuwabara, 2007), suffer from this non-linear force-stress coupling (Upadhyay et al., 2017b). On the other hand, the ISO standard based geometries allow reaching only small amounts of gauge plastic strain prior to failure (Upadhyay et al., 2017b), making them impractical for comprehensive load path change studies.

The full potential of cruciform deformation studies, using the non-ISO standard geometries, can only be realized using a combined experimental-modeling approach. One such synergetic approach was recently proposed (Upadhyay et al., 2016) where a combined *in-situ* neutron diffraction and multi-scale modeling approach allowed to study the macroscale, meso-scale and micro-scale response of the cruciform gauge region during monotonic biaxial loading. At the macroscale, a phenomenological plasticity based finite element (FE) model with combined isotropic and kinematic hardening law was used to simulate the cruciform geometry and estimate the gauge stresses. The predicted gauge stresses were then used as macroscopic boundary conditions to drive an elasto-viscoplastic fast Fourier transform (EVP-FFT) model that is implemented with a Voce type hardening law. This multi-scale approach, however, is only appropriate to study monotonic biaxial loading, primarily due to the hardening laws that are unable to properly capture the macroscopic behavior following a load path change. Recently, Collins and co-workers (Collins et al., 2017) used a crystal plasticity FE based approach to model intergranular strain evolution in their cruciform samples during non-proportional strain path changes. The crystal plasticity FE model was driven under the action of experimental cruciform gauge strains obtained using in-situ digital image correlation. This approach neglects the experimental boundary conditions on the cruciform sample and consequently the non-linear force-stress coupling induced by the cruciform geometry; these govern the intergranular strain evolution in the cruciform gauge region (Upadhyay et al., 2016). Furthermore, this approach relies on the presence of accurate experimental measurements of the gauge strains, which may not always be available for all load path change tests.

In this work, we develop a multi-scale model that captures the role of microstructural evolution (texture, anisotropy, dislocation density, etc.) duing multi-axial load path changes to predict the mechanical response of metal or alloy parts with complex geometries. This model is able to simulate the mechanical response of materials at three length scales: (a) at the macroscopic scale, the sample geometry is modeled using a FE approach to predict the macro-stresses in the cruciform gauge region, (b) at the mesoscopic scale, a polycrystalline model accounts the role of texture, anisotropy and intergranular stress evolution on the macroscopic response, and (c) at the microscopic (slip system) scale, a dislocation density based hardening model for load path changes is implemented to account for slip system hardening. The multi-scale model is developed by combining state-of-the-art modeling approaches at each of these

length scales. The combined model is then applied to study the mechanical response of 316L stainless steel cruciform samples subjected to a uniaxial first load and unload, followed by a reload at different angles in the range (0°, 90°] and a second unload. The multi-scale model allows understanding the effect of a change in loading path on the elastic response, the Bauschinger effect, the elastic-plastic transition regime and the work-hardening response.

1.2. Methodology and scope of the work

We propose to extend the multi-scale approach of (Upadhyay et al., 2016) to allow studying the combined role of anisotropy, texture, and dislocation activity on the multi-axial load path change response of metal and alloy parts with complex geometries.

Firstly, this requires a numerical approach that appropriately simulates the part shape. This can be achieved using the FE approach. Next, appropriate constitutive laws are required to capture the load path change response of the material. To that end, multiple phenomenological plasticity based hardening laws have been proposed. Amongst these, the most sophisticated ones either simulate the internal-stress-induced distortion of yield surfaces during loading or use parameters that capture the microstructural response during different load path changes (Barlat et al., 2011; Feigenbaum and Dafalias, 2014; Freund et al., 2012; Qin et al., 2017; Shi et al., 2017). In this work, the effect of anisotropy, texture and dislocation activity on the macroscopic response is explicitly modeled using a polycrystalline model embedded with a single dislocation density based hardening model for load path changes.

Transmission electron microscopy (TEM) studies on different metals and alloys have reported that the destruction/restructuring of previously formed homogeneous/heterogeneous dislocations structures directly affects the subsequent yield and hardening behavior of the material (Christodoulou et al., 1986; Fernandes et al., 1993; Hasegawa et al., 1975, 1986; Schmitt et al., 1991). Based on these observations, several dislocation density based hardening laws have been proposed to capture the influence of the changing dislocation structures during reversible or non-proportional strain path changes (Beyerlein and Tomé, 2007, 2008; Franz et al., 2009; Holmedal et al., 2008; Peeters et al., 2001). This is achieved by modeling the underlying mechanisms governing dislocation restructuring following an abrupt strain path change. In the present work, we follow the suggestions of Rauch and co-workers (Kitayama et al., 2013; Rauch et al., 2007, 2011, Wen et al., 2015, 2016) who proposed a different approach based on the argument that dislocation structural changes after a strain path change can occur gradually resulting in a transient change in the hardening behavior of the material, for instance during a Bauschinger test. Following Mecking and Kocks (1981), Rauch et al. (2007) extended the classical one-parameter Taylor law relating the flow stress with the square-root of an average dislocation density to a two-parameter law by decomposing the dislocation density into two components, a storage and a recovery term. Next, Rauch et al. (2011) extended this model to simulate the mechanical response during any arbitrary strain path change; this extension is henceforth referred to as the RGBV model, named after the co-authors of that paper. Kitayama et al. (2013) reformulated the continuum RGBV model at the single crystalline length scale to account for slip directionality at the grain level and the role of texture on dislocation activity. This crystallographic reformulation can implicitly “recognize” a strain path change as opposed to explicitly “informing” the model that a strain path change has occurred, as is done in the continuum RGBV approach. Wen et al. (2015) enhanced this model by introducing a back-stress term as a correction to the critical resolved shear stress (CRSS) for each slip system assuming that its effect is to lower the effective CRSS required to activate reversible dislocations in any given slip system. They also proposed to use the crystallographic Taylor law proposed by Franciosi, Zaoui and co-workers (Franciosi et al., 1980; Franciosi and Zaoui, 1982) to account for latent hardening effects arising from anisotropic dislocation-dislocation interactions. The crystallographic extension of the RGBV model (Wen et al., 2015), henceforth addressed as the crystallographic-RGBV model, is used as hardening law in the present work. In comparison to the mechanism based hardening laws, the crystallographic-RGBV model is simpler and avoids explicitly describing and incorporating dislocation structures into the model.

Modeling the role of texture and anisotropy on load path change response of materials requires using a polycrystalline model. To that end, the anisotropic viscoplastic self-consistent (VPSC) polycrystalline model (Lebensohn and Tomé, 1993) is used. The VPSC model in its standalone form (VPSC-SA) was recently implemented with the mechanism based hardening model of Beyerlein and Tomé (Beyerlein and Tomé, 2008) to study texture changes in Beryllium during load path changes (Knezevic et al., 2013a). More recently, the crystallographic-RGBV model was implemented in the standalone VPSC (VPSC-SA) model and successfully used to study the mechanical response of low carbon steel (Kitayama et al., 2013; Wen et al., 2016) and Mg AZ31 alloy (Wen et al., 2015). In the present work, the VPSC-SA model with the crystallographic-RGBV model is used to fit the model parameters.

In order to capture the role of microstructural evolution on the gauge stresses during biaxial load path changes of cruciform samples, the implementation of the VPSC model as a user-subroutine in the ABAQUS implicit FE solver (Patra and Tomé, 2017) is used (henceforth known as VPSC-FE); the VPSC-FE model was originally proposed by (Segurado et al., 2012) and (Knezevic et al., 2013b), and its convergence criterion was modified by (Patra and Tomé, 2017). In this work, the crystallographic-RGBV hardening law is implemented in the VPSC-FE model to allow studying biaxial load path changes on cruciform samples. The viscoplastic and hardening law parameters are fitted, using the VPSC-SA model, to the shear stress vs shear strain curves obtained from shear reverse-shear loading tests performed using the test apparatus presented in (Choi et al., 2015) (see acknowledgements). The same parameters are used for all the VPSC-FE simulations in this work. Biaxial load path change experiments, with the same first load and different reloading angles, are performed on cruciform samples of 316L stainless steel. Cruciform gauge strains are measured using *in-situ* digital image correlation (DIC) technique. The VPSC-FE modeling approach is validated by comparing the simulated cruciform gauge strains with experimental ones. Following this, the mechanical response is analyzed using the predicted gauge stresses.

The concept of iso-plastic potential surfaces (IPPS) or equi-plastic work surfaces has been used by several researchers (Hill et al., 1994; Hill and Hutchinson, 1992; Kuroda and Tvergaard, 1999; Kuwabara et al., 2000; Lowden and Hutchinson, 1975; Phillips and Juh-Ling, 1972) to understand the influence of the plastic deformation history on the subsequent load path change response of

materials. The shape and size of the initial IPPS are determined by the material texture and elastic/plastic anisotropy (Canova et al., 1985). During a load path change, the shape of the IPPS additionally depends on the deformation history and reloading direction. Cruciform samples have already been used to experimentally determine IPPS during biaxial tension and load path changes for different reloading directions; for instance, see (Kuwabara, 2014) and references therein. However, due to buckling problems, the IPPS obtained from cruciform samples are typically restricted to the 1st quadrant of the 2D stress space (with some points in the 2nd and 4th quadrants). In this respect, polycrystalline simulations can be used to generate polycrystalline IPPS (PIPPS) spanning the entire stress space.

PIPPS have already been used to study the behavior of different anisotropic polycrystalline systems at large off-set plastic strain values using the VPSC model for low carbon steel (Jeong et al., 2017), Mg-alloys (Arul Kumar et al., 2017; Steglich et al., 2012), and a Zr-alloy (Lebensohn and Tomé, 1993). It has been shown that the elastic properties of the material can significantly affect the yield behavior immediately after a load path change (Phillips, 1985). While the VPSC approach is useful to determine PIPPS at large strain values, it does not appropriately capture the mechanical behavior of materials in the elastic and elastic-plastic transition regimes. Other modeling approaches such as the Taylor model (Kalidindi and Schoenfeld, 2000), the elastic FFT-based approach (Brenner et al., 2009) or the crystal plasticity FE (Savage et al., 2017) have been used to study PIPPS evolution in different material systems. Here we use the computationally efficient full-field elasto-viscoplastic FFT-based (EVP-FFT) model (Lebensohn et al., 2012) to generate the PIPPS. The EVP-FFT model uses the same viscoplastic law as the VPSC-SA and VPSC-FE models but also accounts for intra-granular distribution of elastic and plastic fields due to grain neighborhoods. In the present work, the crystallographic-RGBV hardening law is implemented in the EVP-FFT model, and the material parameters used are the same as those used for the VPSC-SA and VPSC-FE simulations. It can be argued that a simpler approach than the combined VPSC-FE and EVP-FFT method to obtain cruciform gauge stresses and generate PIPPS would be to use a single multi-scale modeling framework, such as the elasto-plastic self-consistent (EPSC) model (Turner and Tomé, 1994) or the elasto-viscoplastic self-consistent (EVPSC) model (Wang et al., 2010) embedded in a FE framework. However, the EPSC model is a rate-independent model by design but it approximates the rate-dependent (i.e. viscoplastic) response of the material, which is important in this work, through the underlying hardening law. Due to this approximation, it can be difficult to simulate strain softening effects that sometimes occur after load path changes. Meanwhile, the EVPSC model is computationally more intensive than the VPSC model and its implementation in a FE framework would result in significantly higher computational cost rendering it impractical; this is further discussed in section 5.

The paper is organized as follows: The experimental setup and its sources of errors are presented in section 2. Since in this work the crystallographic-RGBV hardening model, VPSC-SA, VPSC-FE and EVP-FFT approaches are used without any modifications to their published algorithms, therefore they are only briefly recalled in the appendix. The procedures for crystallographic-RGBV model parameter identification using VPSC-SA, VPSC-FE meshing and cruciform simulation, and PIPPS generation using EVP-FFT are described in detail in section 3. Section 4 begins with the validation of the simulation procedure. Next, the gauge stress, hardening and PIPPS evolution are analyzed to understand the mechanical behavior for different biaxial load path changes. The microstructural origin of the mechanical behavior is discussed in section 5. Furthermore, this section also presents the advantages, disadvantages and the applicability of the multi-scale modeling framework used in this work. The main conclusions of this study are presented in section 6.

2. Experimental setup

In this section, the shear reverse-shear and cruciform load path change experiments used to fit the crystallographic-RGBV hardening parameters and validate the VPSC-FE model, respectively, are discussed. Both the models are described in the appendix.

2.1. Material

The as-received material is a warm rolled sheet of face centered cubic (fcc) 316L austenitic stainless steel composed of: Cr-17.25, Ni-12.81, Mo-2.73, Mn-0.86, Si-0.53, C-0.02 (weight %). The sheet is 10.5 mm thick and has in-plane dimensions of 2000 mm × 1000 mm.

Preliminary characterization tests were performed to analyze the material. Electron backscattering diffraction (EBSD) analysis of the as-received sample reveals a mild texture with an average grain size of 7μm. In-situ neutron diffraction tests were performed during uniaxial tensile loading of dog-bone samples prepared along the rolling direction (RD) and transverse direction (TD). Both samples exhibit nearly the same lattice strain response and macroscopic stress-strain response, indicating that the mild texture has a negligible influence on the multi-scale mechanical response. The details and results of these tests are presented in (Van Petegem et al., 2016).

2.2. Sample geometries

Fig. 1a and b show the sample geometry and dimensions used for the shear reverse-shear test and cruciform load path change tests, respectively. The sample outlines are water cut from the 316L sheet and the final geometry is obtained by mechanical milling. The thickness tolerance for these samples is ± 0.05 mm. All the samples are prepared such that the RD and the TD are always aligned along directions 1 and 2, respectively.

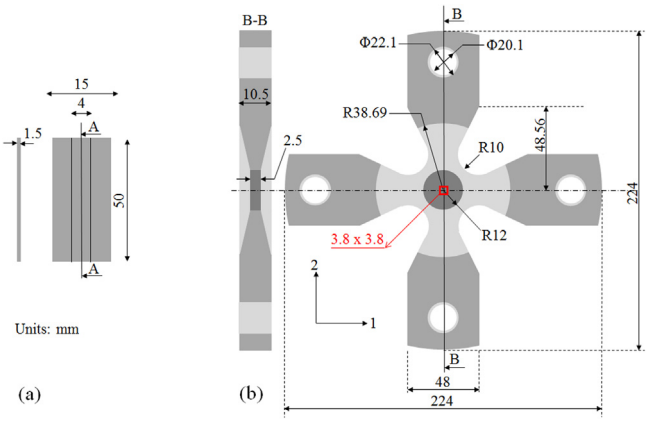

Fig. 1. (a) Cuboid sample used for the shear reverse-shear experiments (Choi et al., 2015). (b) Cruciform geometry used for biaxial load path change experiments. The area of interest (gauge) at the center of the cruciform sample is marked in red. The RD and the TD for both samples are aligned along directions 1 and 2, respectively, shown in (b). (For interpretation of the references to color in this figure legend, the reader is referred to the Web version of this article.)

2.3. Mechanical tests

The shear reverse-shear tests were performed using the simple shear test device in the laboratory of Prof. Frédéric Barlat at POSTECH, Republic of Korea. The rectangular shaped sample was clamped along its longitudinal direction using two rigid grips. One of the grips is immobile while the other moves only along the longitudinal direction. As seen in Fig. 1a, the sample has the dimensions of $50 \times 15 \times 1.5\,\text{mm}^3$. The grips clamp a significant portion of the sample resulting in a deformation area of $50 \times 4\,\text{mm}^2$. In order to eliminate high strain gradients in the gauge area due to the effects of clamping, a gauge area of $16 \times 4\,\text{mm}^2$ was chosen at the center of the $50 \times 4\,\text{mm}^2$ area. This choice was made based on a previous study (Choi et al., 2015) where it was shown that the deformation is nearly uniform in this smaller region. In order to prevent slippage due to insufficient pressure, the entire specimen is encapsulated in a serrated groove; the design of this groove and further details on the machine can be found in (Choi et al., 2015). The shear reverse-shear test is performed in displacement control with a rate of 0.001 mm/s resulting in a strain rate of $0.00025/s$. The sample is subjected to forward (positive) shear loading up to 8% shear strain and then reverse (negative) loading up to -4% shear strain. The true shear stress vs true shear plastic strain curve is shown (in black) in Fig. 2. The corresponding simulation conditions and resulting parameters are presented in Section 3.1.

Cruciform samples are deformed using a biaxial deformation rig with independent arm control. The rig allows deforming in tension/compression up to 50kN along direction 1 and 100kN along direction 2. The rig deforms the cruciform using grips comprised of bolts that slide into the holes in the cruciform arms. For a detailed description of the machine, the interested reader is referred to (Van Petegem et al., 2016).

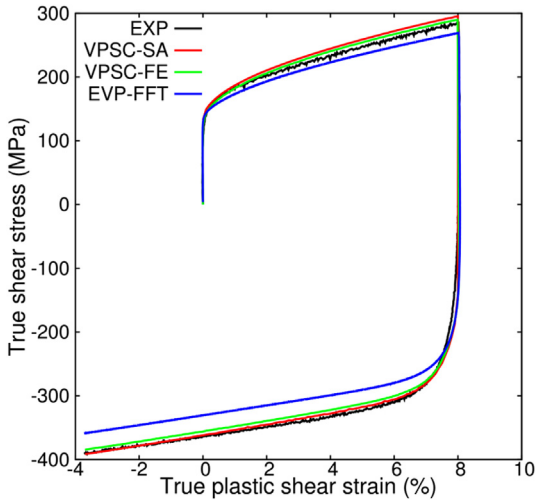

Fig. 2. Comparison of the true shear stress vs plastic shear strain curves obtained from shear reverse-shear experiment (in black), and VPSC-SA (in red), VPSC-FE (in green) and EVP-FFT (in blue) simulations. (For interpretation of the references to color in this figure legend, the reader is referred to the Web version of this article.)

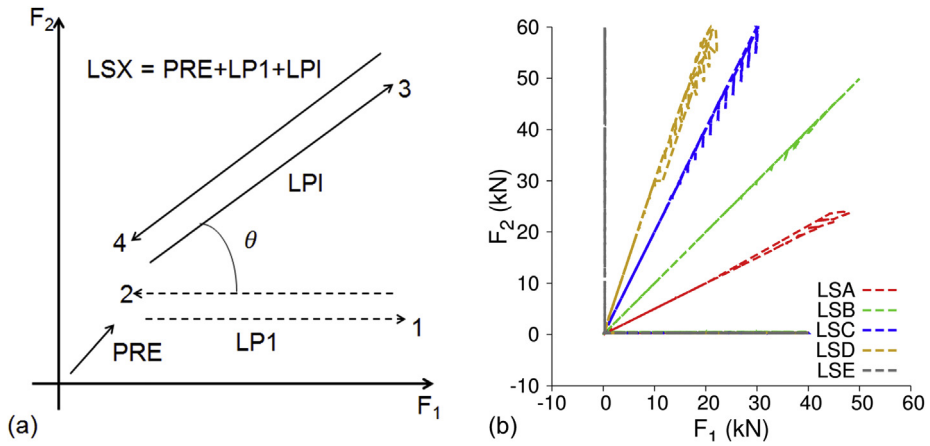

Fig. 3. (a)–(e) Schematics (not to scale) showing load path changes during each LSX (X = A–E) = PRE + LP1 + LPI (I = 2–6), respectively, in the 2D force space. (f) Experimental applied forces for different LSX including force relaxations during displacement holds for in-situ neutron diffraction measurements.

We have performed five different biaxial tensile load path change tests on the cruciform samples; note that these tests are different from any tests reported in our previous studies (Upadhyay et al., 2016, 2017a; 2017b; Van Petegem et al., 2016). Prior to the first loading sequence, all cruciform samples are gripped in the machine by applying a small equi-biaxial pre-load (PRE) of 0.3kN to avoid slippage during load path changes. Next, for all cruciform samples, F_1 is increased to 40kN followed by a decrease back to 0.3kN. Henceforth, this loading and unloading sequence will be referred to as load path 1 (LP1). During LP1, F_2 is kept constant at 0.3kN which makes LP1 a nearly uniaxial loading and unloading sequence. Following LP1, each cruciform sample is subjected to separate load path changes with ratios, (a) F_1: F_2 = 2: 1, (b) F_1: F_2 = 1: 1, (c) F_1: F_2 = 1: 2, (d) F_1: F_2 = 1: 3, and (e) F_1: F_2 = 0: 1, and then all samples are unloaded back to 0.3 kN along both arms while maintaining their respective load ratios. These five different loading and unloading paths will be referred to as LPI (I = 2 to 6). An illustration of the combined loading sequence of PRE + LP1 + LPI (I = 2 to 6), henceforth designated as LSX (with X = A to E), is shown in Fig. 3a. During the loading and unloading, the direction of higher force is always loaded/unloaded at a force rate of 80 N/s and the force rate along the other direction is adjusted according to the desired load ratio.

During each LSX, in-situ neutron diffraction measurements were performed at regular force intervals. During these measurements, the loading or unloading sequence is stopped and the cruciform arms are held at constant displacement for ~15 min. A detailed analysis of these neutron diffraction measurements will be presented in a separate work. In this work, we account for the role of this displacement hold on the mechanical response of 316L cruciform samples. During this hold period, the applied forces in the cruciform arms either remain constant (in the elastic regime) or relax to lower values (following onset of plasticity). Immediately after the displacement hold, the samples are loaded back to the force values just before the beginning of that displacement hold. During this reloading, the force rates are adjusted such that the forces along both axes reach their final values at the same instant. Note that these re-loading rates can be different from the desired loading rates for a given load path because the force relaxations do not follow the loading ratio of that load path. Following this, the loading rates are changed back to the desired ones and the loading sequence continues.

Fig. 3b shows the experimental F_2 vs F_1 curve for all the LSX. The true maximum force values during the different LPI are as follows: a) LP2 – F_1: F_2 = 48kN : 24.4kN, b) LP3 – F_1: F_2 = 50kN : 50kN, c) LP4 – F_1: F_2 = 60kN : 31.4kN, d) LP5 – F_1: F_2 = 59.9kN : 20.9kN, and e) LP6 – F_1: F_2 = 59.7kN : 0.3kN. The true reloading angles θ, as shown in Fig. 3a, are 27°, 45°, 62°, 71° and 90°, respectively; the values are rounded to nearest integers.

Cruciform in-plane gauge strain measurements are performed using the digital image correlation (DIC) technique. A two-camera ARAMIS4M® DIC system from GOM is installed on the biaxial rig to perform in-situ measurements of surface strains on the cruciform gauge area. All the DIC strains reported in this work are averaged over the gauge area of 3.8 × 3.8 mm^2 at the center of the cruciform surface as shown in Fig. 1b. The averaging procedure is motivated from in-situ neutron diffraction experiments where the diffraction patterns are obtained from the gauge region which is the through thickness volume beneath the 3.8 × 3.8 mm^2 area (Upadhyay et al., 2016, 2017a; Van Petegem et al., 2016). The speckle pattern, necessary for DIC measurements, is prepared by hand spraying the gauge surface with black and white paint in the sequence: black-white-black.

2.4. Sources of error in experimental data

1) The machining tolerance of ± 0.05 mm for the cruciform gauge region may result in differences in the gauge strain for different samples subjected to the same loading sequence. The impact of this thickness tolerance will be discussed in the results section 4.
2) The warm-rolled 316L sheet exhibits differences in the texture at the center with respect to the edges of the sheet. This implies that the cruciform samples may have different starting textures, and consequently different mechanical response.

Table 1
Parameters of the viscoplastic power law (equation (A6)) and crystallographic-RGBV hardening law (equations A1, A2, A4 and A5) fitted to the shear reverse-shear test results shown in Fig. 2.

Viscoplastic power law	
$\dot{\gamma}_0$ (Reference shear rate)	$1\ s^{-1}$
n (Power law exponent)	20
crystallographic-RGBV model	
τ_0^s (Initial CRSS for all slip systems)	123 MPa
μ (Shear modulus)	85000 MPa
b (magnitude of Burgers vector)	2.5243 A^0
$\alpha^{ss'}$ (dislocation-dislocation interaction matrix)	0.2 $(s = s')$
	0.45 $(s \neq s')$
ρ_{min} (Lower reversibility threshold)	$10^{11}\ m^{-2}$
ρ_{max} (Upper reversibility threshold)	$10^{14}\ m^{-2}$
f (Recovery parameter)	1
m (Recombination rate parameter)	14
K (Mobile to storage parameter)	158
D (Grain size)	$7\ \mu m$
f_B^s (back-stress parameter)	0.5
q (back-stress parameter)	12

3) The error associated with the DIC measurement for the cruciform and dog-bone samples is given using the equation: $err(\%) = a \times \text{strain}(\%) + b$; where a and b are in the range [0.014, 0.024] and [0.05, 0.09], respectively. For example, at 10% strain the maximum error in the DIC strain is 0.33%.

3. Simulation details

3.1. Material model parameters

In previous works on biaxial deformation of cruciform samples using the EVP-FFT approach (Upadhyay et al., 2016, 2017a), a synthetic representative volume element (RVE) composed of 2500 equiaxed grains with random texture was used to approximate the mild texture associated with the 316L steel. In the present work, the same microstructure is used for the EVP-FFT simulations. The RVE is divided into 16^3 equi-spaced voxels in 3D space. Note that in the work of (Upadhyay et al., 2016, 2017a), 64^3 equi-spaced voxels were used to discretize the RVE. In this work, we are only interested in the macroscopic response of the material, specifically the PIPPS, and there are no significant differences in this response of the RVE with 16^3 voxels or 64^3 voxels. Each voxel belonging to the same grain is assigned the same initial orientation associated with that grain. For the VPSC-FE simulations, to improve computational efficiency, a reduced 100-grain random texture is used.

The VPSC-SA and VPSC-FE (EVP-FFT) simulations are performed by assigning single crystal plastic properties (and also elastic properties for EVP-FFT) of 316L steel to every grain (voxel). The plastic response of the fcc 316L stainless steel is modeled using the rate-sensitive viscoplastic constitutive relationship in equation (A6) assuming one active slip mode with dislocation glide on 12 {111}<110> slip systems. Due to its computational efficiency, VPSC-SA is used to fit the unknown parameters of the hardening law, equation (A2), and the viscoplastic strain rate law parameters, equations (A4), (A5) and (A6). There are 15 parameters that need to be identified and are shown in Table 1. Amongst them, τ_0^s, f, m, K, f_B^s and q are fitted using the true shear stress vs true plastic shear strain curve shown in Fig. 2. The remaining parameters $\dot{\gamma}_0$, n, μ, b, α^{ss}, $\alpha^{ss'}$, ρ_{min}, ρ_{max} and D are fixed based on the knowledge of the material and assumptions from previous studies where these equations have been used. Note that the cruciform tests are not used for fitting these parameters because of the complexity associated with the boundary conditions and sample thickness variations in the cruciform test; these reasons will become apparent in section 4.1. The strain-rate component $\dot{E}_{12} = 0.00025\ /s$ was imposed and all the other strain rates were imposed to zero. After reaching the experimental plastic shear strain during forward shear, $\dot{E}_{12} = -0.00025\ /s$ was imposed. The fitted parameters are shown in Table 1. These parameters are used in all the simulations performed in this work using the three models: VPSC-SA, VPSC-FE and EVP-FFT.

For the EVP-FFT simulations, each voxel is also assigned the single crystal elastic properties for 316L stainless steel. Similar to previous works (Upadhyay et al., 2016, 2017a), the 3 independent single crystal elastic constants for the fcc 316L stainless steel are taken as: $C_{11} = 204.6$ GPa, $C_{12} = 137.7$ GPa and $C_{44} = 126.2$ GPa (Gonzalez et al., 2012). The EVP-FFT model predicted response for the shear reverse-shear test is shown in Fig. 2 in blue. The hardening response is under-predicted. In EVP-FFT, the intra-granular stresses are accommodated via both elastic and plastic strains resulting in a lower macroscopic hardening response. The percentage difference in shear stress at the end of reverse loading is less than 10%. Since the EVP-FFT model will be used to generate PIPPS at low strain values, the same parameters can be used without incurring any significant errors; at larger strains, these parameters would have to be refitted.

In the VPSC-FE code, the macroscopic elastic stiffness is required to compute the macroscopic elastic strains. The VPSC code has a subroutine that computes the self-consistent elastic stiffness from the single crystal elastic constants presented above. This stiffness is

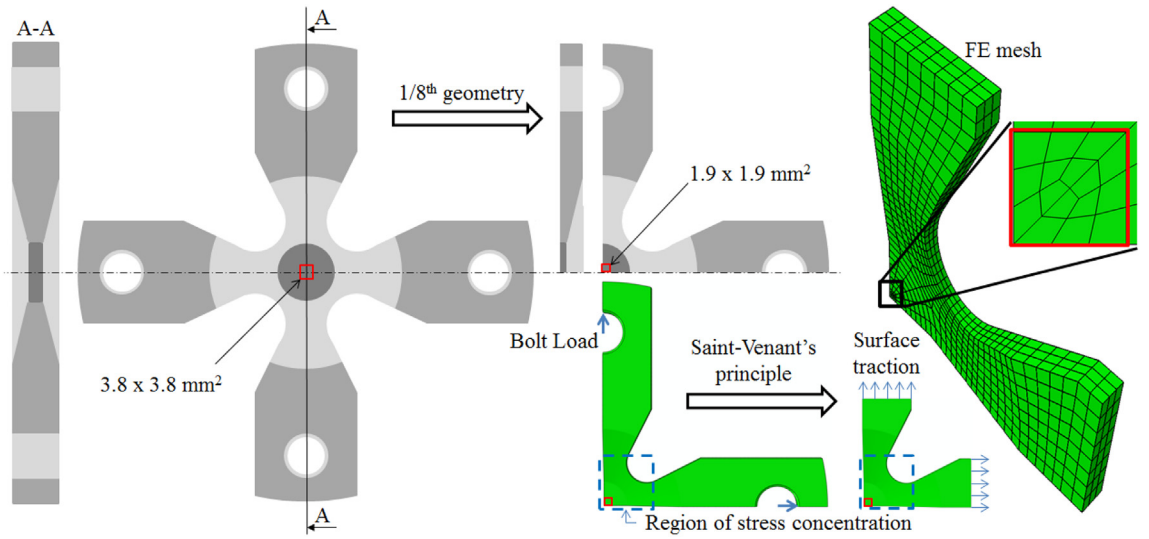

Fig. 4. Procedure to generate the FE mesh for cruciform simulations in ABAQUS. The cruciform geometry shown in Fig. 1b is cut along its symmetric planes and reduced to a 1/8th part. Saint-Venant's principle is used to further reduce the cruciform geometry by cutting off a portion of the arms and replacing the original bolt load by a surface traction on the newly cut surfaces. The final geometry is meshed using hexahedron linear elements with reduced integration. The gauge region is the area demarcated by the red box and the volume underneath this box. (For interpretation of the references to color in this figure legend, the reader is referred to the Web version of this article.)

not used in the VPSC algorithm but it is used to estimate the value of $\overline{\boldsymbol{C}}$ that enters in equations (A10), (A11) and (A14) of the VPSC-FE code. The predictive capability of the VPSC-FE model is also tested for the shear reverse-shear test. A single linear mesh element having 1 integration point is used. Fig. 3 shows (in green) the true shear stress vs plastic shear strain response predicted by VPSC-FE. This response is slightly softer and harder than the VPSC-SA and EVP-FFT predictions, respectively, and matches well with the experimental curve. This validates the VPSC-FE implementation in ABAQUS.

3.2. VPSC-FE mesh and simulation setup

For better computational efficiency of the VPSC-FE cruciform simulations, only 1/8th part of the cruciform geometry (shown in Fig. 4) is simulated with appropriate symmetric boundary conditions imposed on the cut surfaces. A structured hexahedron mesh with linear 8-node mesh elements and reduced integration points (C3D8R in ABAQUS) is used; hourglass stiffness is set to 205. Each integration point in the mesh is representative of the 100-grain microstructure and the local mechanical response is computed using the VPSC approach via the VPSC-FE code. In accordance with the experiments, the different load path change simulations are performed in load control with the same force rate values and biaxial load ratios as in the experiments.

The viscoplastic power law and crystallographic-RGBV model parameters are the same as those used in Table 1. The VPSC-FE code also requires prescribing the total number of state variables used at each integration point for VPSC computations. For an N-grain microstructure, $\sim 150N$ state variables need to be computed and stored per integration point, making the simulation computationally expensive. For additional gains in computational efficiency, Saint-Venant's principle can be invoked to further reduce the cruciform geometry. This principle allows replacing a static load that is sufficiently far away from regions of stress concentrations with another equivalent static load that is also sufficiently far away from the stress concentrations. In the cruciform geometry, the stress concentrations occur in the region shown within the blue box in Fig. 4. Furthermore, the cruciform arms deform elastically during the course of loading. Therefore, based on the Saint-Venant's principle, the simulated cruciform geometry can be shortened in the arms and the bolt load can be transformed into a statically equivalent uniform surface traction as shown in Fig. 4. The cruciform arms were cut at a 5 mm distance from the location of the change in arm width. This distance was arbitrarily chosen and test simulations with cuts at 4 mm and 6 mm show no significant change in the location or magnitude of stress concentrations. The final FE mesh consists of 1236 elements.

Consistent with the experiments, all the cruciform loading simulations were performed in force control. As a proof of concept, displacement holds were also simulated to show the effect of such holds on the material's hardening behavior. To that end, the surface traction loading condition is replaced with a zero velocity boundary condition along that direction. These holds result in plastic strain increments that are accompanied by force relaxations. Capturing the strain increments during displacement holds also requires implementing a creep law which is beyond the scope of the present work. As will be shown later in the results section 4.1, the error associated with neglecting these strain increments is acceptable since these increments are less than 0.5% strain. It is however noteworthy that the viscoplastic power law has previously been used to simulate the creep response using a different value for the exponent n, see for instance (Wang et al., 2013). In this work, for all simulations, n is kept constant and equal to 20 throughout the simulation. Consequently, the simulated and experimental force relaxations occur during different time scales. The duration of each

displacement hold is set to 0.8 secs. Following these holds, the cruciform is immediately reloaded with the desired loading rates.

At the end of each simulation, the applied forces in the arms and predicted gauge surface strains are extracted and compared with their corresponding experimental measures. The simulated force evolution is obtained by extracting appropriate stress components from the outermost mesh elements in the arms; taking their mean, and multiplying it with the cross-sectional area. The gauge strain components are extracted from the 16 outermost mesh elements (in the out-of-plane direction) that lie within the 1.9×1.9 mm^2 surface area shown in Fig. 4. The components are averaged over these elements and this average is compared with the average of the DIC strains from the 3.8×3.8 mm^2 surface area shown in Fig. 1b. Gauge stresses are extracted from the 48 through-thickness mesh elements underneath the 1.9×1.9 mm^2 region. These stresses are averaged and their evolution is studied. The averaged stresses are also used as macroscopic boundary conditions to drive the EVP-FFT simulations.

All the VPSC-FE simulations were performed on the Deneb cluster in the high performance computing facility of the Ecole Polytechnique Fédérale de Lausanne. Each simulation was executed in parallel on a single node using 16 cores. The total simulation time depends on the number of mesh elements, the number of internal state variables that are processed by the VPSC-FE interface, and the VPSC algorithm to compute these state variables. In the current simulation setup, the number of state variables per integration point are: 196 + 51∗(# *of grains*) + (8∗(# *of slip systems*) + 1)∗(# *of grains*); the first term is due to the VPSC-FE interface, the second term is due to the VPSC algorithm, and the third term is due to the RGBV model. Therefore, for the 100-grain texture, the number of state variables per integration point is 14996 and the total number of state variables for each simulation is $\sim 18.5 \times 10^6$. With these model requirements and the available computational resources, the average execution time for an LSX simulation is $\sim$ 50 hours.

3.3. Generating PIPPS

Following the work of (Lebensohn and Tomé, 1993), a PIPPS contour is defined as an equal plastic work rate or dissipation rate ($\dot{W}^p$) contour generated from polycrystalline plasticity simulations and satisfies the following condition:

$$\dot{W}^p = \dot{\mathbf{E}}^{\boldsymbol{vp}} : \boldsymbol{\Sigma} = \dot{\varepsilon}_{ij}^{vp} \sigma_{ij} = constant \tag{1}$$

where $\dot{\mathbf{E}}^{\boldsymbol{vp}}$ is the weighted average of the local viscoplastic strain rates computed using equation (A6). The PIPPS are generated by probing along different directions in the 2D strain rate space.

PIPPS calculations are performed for the initial un-deformed microstructure, microstructure after PRE + LP1, and the microstructures at the end of different LSX. We use the 2500-grain initial microstructure that was used for the EVP-FFT simulations in (Upadhyay et al., 2016). This microstructure provides more numerical stability during PIPPS computations than the 100-grain microstructure that was used for the VPSC simulations. Furthermore, comparison of the PIPPS constructed from both microstructures does not reveal any significant differences. In order to compute the PIPPS after a particular load sequence, the initial 2500-grain microstructure used for EVP-FFT simulations needs to be brought to the deformed state at the end of that loading sequence. However, in this work, the EVP-FFT model is used in its stand-alone form. This model is unable to account for the non-linear force-stress coupling that arises from the complex cruciform geometry. In order to overcome this issue, the VPSC-FE predicted cruciform gauge stresses for a given LSX are used as macroscopic boundary conditions to drive the EVP-FFT simulations for that LSX; this procedure provides significant gains in computational time over using the implementation of EVP-FFT as a user-material in ABAQUS. Using this procedure, the 2500-grain microstructure is brought to the same macroscopic stress state as the 100-grain microstructure from VPSC-FE simulations at the end of a given LSX. This multi-scale procedure is motivated by the works of (Upadhyay et al., 2016, 2017a) where it was used to study intergranular strain evolution during uniaxial and equibiaxial loading of 316L cruciform samples. At the end of each simulation, restart files containing the final state of the microstructure are generated. These files are then used as the reference state of the microstructure to generate PIPPS.

PIPPS simulations are performed by imposing a macroscopic total strain rate tensor whose norm $|\dot{\mathrm{E}}|$ is fixed to 10^{-3}/s. The strain rate components $\dot{\mathrm{E}}_{11}$ and $\dot{\mathrm{E}}_{22}$ are imposed to be non-zero whereas $\dot{\mathrm{E}}_{33}$ is not imposed. In contrast, Σ_{33} is imposed to be zero whereas Σ_{11} and Σ_{22} are allowed to adjust according to their constitutive relationships with the strains. All shear strain rates are imposed to zero which ensures that the shear stresses, even though not imposed, are negligible. This is later confirmed for all PIPPS computed in this work; for all the simulations, the absolute value of any of the shear stress components never exceeds 10 MPa and at any time step they are less than 10% of the magnitude of the in-plane normal stresses. These conditions imply that the imposed strain rate tensor norm $|\dot{\mathrm{E}}| = \sqrt{(\dot{\mathrm{E}}_{11})^2 + (\dot{\mathrm{E}}_{22})^2}$ is equal to $10^{-3}/s$. The 2D strain rate space is divided in 72 equi-angular ($\Delta\theta = 5°$) probing directions such that $\dot{\mathrm{E}}_{11} = |\dot{\mathrm{E}}| \cos\theta$ and $\dot{\mathrm{E}}_{22} = |\dot{\mathrm{E}}| \sin\theta$. Along each probing direction, at time $t + \Delta t$, the imposed strain E_0 is computed as $\mathrm{E}_0^{t+\Delta t} = \mathrm{E}_0^t + |\dot{\mathrm{E}}^{t+\Delta t}|\Delta t$. Note that since the EVP-FFT model is used to compute the PIPPS, E_0 contains both elastic and plastic strain contributions. A reference dissipation rate $\dot{W}^p_{ref} = 1$ MPa/s is chosen. To achieve this desired dissipation rate, at every time increment Δt along a probing direction, the strain rate components are scaled by a factor $(\dot{W}^p_{ref}/\dot{W}^p_{actual})^{\frac{n}{1+n}}$ and the stresses are scaled as $(\dot{W}^p_{ref}/\dot{W}^p_{actual})^{\frac{1}{1+n}}$; where n is the viscoplastic power law exponent. This fulfils the condition in equation (1) which also ensures that the PIPPS coincide with the macroscopic yield surface (Lebensohn and Tomé, 1994). PIPPS are then generated by plotting the scaled stress components Σ_{11} and Σ_{22} in the 2D stress space for different values of E_0. Note that the PIPPS computations can also be performed by imposing a stress rate instead of a strain rate; the shape of the PIPPS thus obtained would be different from those obtained by imposing constant strain rate.

The computational procedure to generate PIPPS is as follows:

i) Initialize the simulation parameters and state variables from the restart file.
ii) Probe with $|\dot{E}|$ along a certain direction in the 2D strain rate space.
iii) At pre-selected values of E_0, output the scaled strain rate and stress values.
iv) Repeat steps (i)-(iii) for all the probing directions.

Customarily, yield points are determined at 0.2% offset plastic strain in uniaxial experiments. At this amount of plastic strain, the role of kinematic hardening on the yield surface evolution may have considerably diminished and the yield surfaces may be evolving in a homothetic manner (same shape but different size). However, yield surfaces constructed at smaller offsets have shown large deviations from homothetic expansion (Phillips, 1985) and are of particular interest to study the extent of Bauschinger effect in the material after load path changes.

Note that E_0 is taken as a measure of total strain and not the plastic strain; the reasons for this choice will become apparent at the end of section 4 and are explained in section 5. The as-received 316L stainless steel has the Young's modulus of 190 GPa and the uniaxial tensile yield stress of 280 MPa (Upadhyay et al., 2016). This gives a total strain of 0.35% for the 0.2% offset plastic strain. Bearing this in mind, the PIPPS evolution will be studied at the following E_0 values: 0.1%, 0.2%, 0.35%, 0.5%, and 1%. The reasons for studying the PIPPS at E_0 = 0.5% and 1% will be evident in section 4.3.

4. Results

4.1. Experiment-simulation comparison

The PRE load applied to grip the samples results in negligible strain increments in comparison to those occurring during LP1 and different LPI loadings. During LP1 loading, the maximum applied force F_1 (40kN) and force rate (80N/s) on all cruciform samples are the same, however, there is a non-negligible difference in their measured E_{11} values. At the end of LP1, the largest difference in measured E_{11} (0.01381) occurs between the cruciform samples subjected to LSA and LSC loadings; note that this difference is one of the key reasons the cruciform tests are not used to fit the hardening law parameters (see section 3.1). The experimental F_1 vs E_{11} curves for the PRE + LP1 sequences during LSA and LSC are shown in Fig. 5.

The origin of this difference can be ascribed to the gauge thickness tolerance of 2.5 ± 0.05 mm mentioned in section 2.4. To prove this, three LP1 simulations with displacement holds are performed for three cruciform gauge thicknesses: 2.45mm, 2.50mm and 2.55mm. All other dimensions and simulation parameters are kept the same. For each simulation, the displacement holds are performed at four forces: F_1 = 24kN, 30kN, 35kN and 40kN; these values correspond to the pre-selected experimental forces at which the displacement holds are performed for the LP1 of each LSX (except LSB). Only the F_1 vs E_{11} curve from the simulated 2.5mm thick cruciform geometry with displacement holds is shown in green in Fig. 5. At the end of LP1, the predicted E_{11} from the 2.5 mm thick cruciform simulation is found to be close to that obtained during LSC. The predicted E_{11} for the 2.45 mm and 2.55 mm thick cruciform simulations are found to have relatively larger and smaller values, respectively (not shown in figure); at the end of LP1, the difference in their predicted E_{11} is 0.0093. Simulations were also performed for different loading rates and other random textures but in comparison with the strain differences arising from changing gauge thickness, these have negligible contributions.

Fig. 5 also shows the F_1 v/s E_{11} curve obtained from the simulated 2.5mm cruciform geometry without displacement holds (in red). At the end of LP1, E_{11} values are higher than those predicted for the simulation with displacement holds. This is because after the displacement hold, the gauge stress Σ_{11} reaches its previous highest magnitude with a steeper hardening rate. Therefore, at the same E_{11}, the subsequent strain increment is smaller in the simulation with displacement hold compared to the simulation without displacement hold. The difference in strains between 2.5mm thick cruciform simulations with and without displacement holds increases with increasing strain and the number of displacement holds. These differences are acceptable considering the influence of the

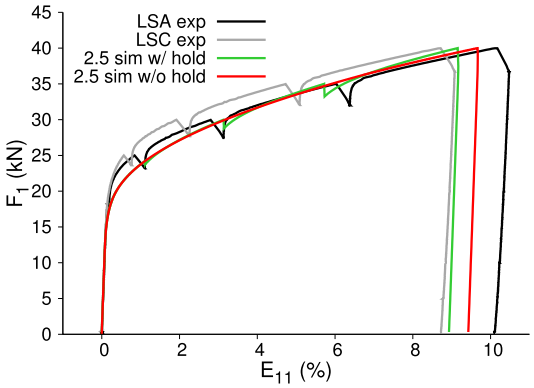

Fig. 5. The experimental $\mathbf{F}_1$ (kN) vs $\mathbf{E}_{11}$ (%) curves for PRE + LP1 of LSA (in black – highest $\mathbf{E}_{11}$ amongst all LP1 of LSX) and LSC (in grey – lowest $\mathbf{E}_{11}$ amongst all LP1 of LSX) are compared with the simulated $\mathbf{F}_1$ vs $\mathbf{E}_{11}$ curves for the 2.5mm gauge thickness cruciform with (in green) and without (in red) displacement holds. (For interpretation of the references to color in this figure legend, the reader is referred to the Web version of this article.)

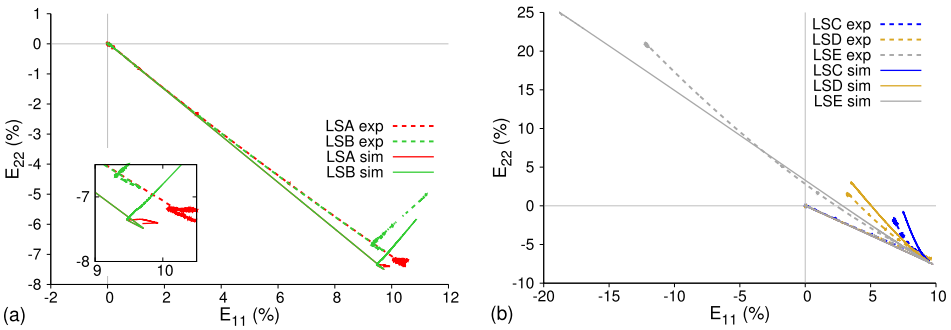

Fig. 6. Comparison between experimental and VPSC-FE predicted E_{22} vs E_{11} for (a) LSA and LSB, and (b) LSC, LSD and LSE. For LSA, the strain values after reloading are very small and can be better visualized through the inset in (a).

thickness tolerance on the strain values. Despite these differences, the simulated strains from 2.5mm thick cruciform without displacement holds lie within the bounds of the spread in experimental strain values. In light of the above, all the VPSC-FE simulation results shown in the rest of this article will be obtained from simulations performed on 2.5mm gauge thickness cruciform geometries without displacement holds. Note that, the complexity associated with simulating these displacement holds is another reason for not using the cruciform tests for fitting the hardening law parameters (see section 3.1).

Fig. 6 shows for all LSX the plot of E_{22} vs E_{11} obtained from simulations and DIC measurements. At the end of LP1 for all LSX, the DIC measured strain components E_{11} and E_{22} are in the range [0.0865, 0.1003] and [−0.0737, −0.0634], respectively, whereas their respective simulated values are equal to 0.0947 and − 0.0736. Following PRE + LP1, the strain evolution is different for all LSX. In general, the percentage difference between simulated and DIC strains is lower for E_{11} than for E_{22}. LSA and LSE result in the smallest and largest change in strain after LP1, respectively. LSA and LSB show positive increments in both strain components during reloading after PRE + LP1. LSC, LSD and LSE on the other hand show positive increments in E_{22} and negative increments in E_{11}. These trends in strain evolution are well captured by the simulations. However, as expected the predicted strain values are different from the measured DIC strains. The largest deviation in simulated strains with respect to DIC strains occurs for LSE; it is 34.5% and 18.4% for E_{11} and E_{22}, respectively (starting from the end of LP1 to the end of LSE). Note that these differences are found to diminish considerably when the DIC strains are compared with those obtained from a 2.55 mm gauge thickness cruciform simulation with displacement holds (not shown here).

Fig. 7 shows the experimental and simulated F_1 vs E_{11} and F_2 vs E_{22} plots for all LSX. Simulations capture well the force-strain evolution for all LSX. During reloading after LP1, LSA exhibits the hardest F_1 vs E_{11} response, which is significantly more than during

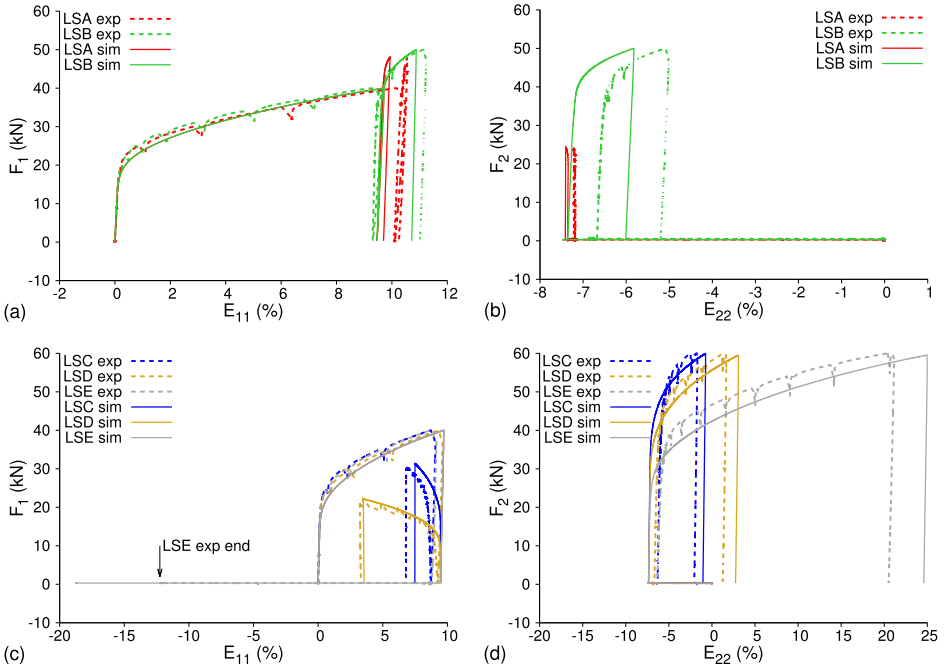

Fig. 7. Comparison between experimental and simulated (a, c) F_1(kN) vs E_{11} (%), and (b, d) F_2 (kN) vs E_{22} (%), plots for all (a, b) LSA and LSB, and (c, d) LSC, LSD and LSE.

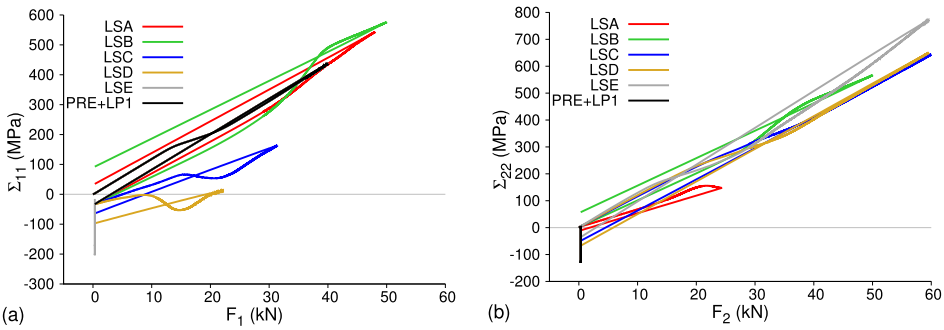

Fig. 8. Simulated (a) Σ_{11} vs F_1 and (b) Σ_{22} vs F_2 for all LSX. For clarity, PRE + LP1 for each LSX is highlighted in black.

LP1. The F_1 vs E_{11} response progressively softens from LSA to LSE and changes sign at LSC. In contrast, the F_2 vs E_{22} response hardens from LSA to LSB and then softens to LSE. Note that due to the non-linear coupling between applied forces and gauge stresses, the force-strain evolution may not be representative of the stress-strain hardening behavior of the material.

It is well-known that for 316L stainless steel dog-bone samples that $^{E_{22}}/_{E_{11}}$ equals − 0.31 in the elastic regime and − 0.5 in the plastic regime. However, this is different for a cruciform geometry. Simulations of LP1 loading show that $^{E_{22}}/_{E_{11}} = -0.42$ in the elastic regime and $^{E_{22}}/_{E_{11}} = -0.77$ at the end of loading. This implies that during uniaxial loading along direction 1 of the cruciform sample, in addition to the tensile stress Σ_{11} the gauge area is subjected to a compressive stress Σ_{22}. Such a biaxial cruciform gauge stress state for a similar cruciform geometry has previously been reported in literature and analyzed in the elastic regime (Bonnand et al., 2011; Cláudio et al., 2014), and has been studied in detail in the plastic regime (Upadhyay et al., 2017b).

Following the onset of plasticity, the applied forces become non-linearly coupled to the gauge stresses, and the evolution of this non-linearity depends on the cruciform geometry shape, applied loading ratio, and the material properties (Upadhyay et al., 2017b). This makes it difficult to analytically extract gauge stress evolution and study the hardening behavior of the material. Therefore, in the next section, the simulated stresses are analyzed for the different load path changes.

4.2. Mechanical response during biaxial load path changes

Simulations for all LSX reveal that the gauge stress state is always biaxial in-plane, i.e. Σ_{11} and Σ_{22} are non-zero; all other stress components were found to be less than 13 MPa in magnitude, and at any time step during any LSX, their absolute value is less than 7% of the absolute values of Σ_{11} and Σ_{22}. This allows us to perform the stress analysis in the 2D $\Sigma_{11} - \Sigma_{22}$ stress space. Fig. 8a and b show respectively the Σ_{11} vs F_1 and Σ_{22} vs F_2 curves for all LSX (PRE + LP1 is highlighted in black). The equibiaxial PRE loading $F_1 = F_2 = 0.3$kN results in $\Sigma_{11} = 2.92$ MPa and $\Sigma_{22} = 3$ MPa which is negligibly small in comparison to the stresses achieved after PRE; this slight difference in stresses is a consequence of the limited number of grains contained in the RVE (100 grains) which results in a slightly anisotropic macroscopic elastic response.

During LP1 loading, although F_2 is fixed at 0.3kN and only F_1 increases to 40kN, Σ_{22} reaches a value of − 131MPa. This confirms, as discussed in the introduction section 1.1, that under uniaxial loading without any deformation history, the cruciform gauge region is in a biaxial stress state with a non-negligible in-plane compressive component normal to the loading direction. During LP1, the elastic-plastic transition regime is characterized by a distinct non-linear kink in the Σ_{11} vs F_1 evolution. After LP1, the stress response during the reloading for all LSX also results in a complex non-linear coupling between both the applied forces and the gauge stresses. During reloading after LP1, the non-linearity in Σ_{11} vs F_1 appears to be increasingly pronounced going from LSA to LSD. For LSE, Σ_{11} decreases during reloading even though there is no increase in F_1. These results underline the role of the cruciform geometry in determining the stress evolution during load path changes, particularly in the elastic-plastic transition regime. In addition to the geometry, the magnitude and direction of the applied forces play an important role in stress evolution. For instance, under the same reloading force $F_2 = 60$ kN, LSD and LSE result in different non-linear Σ_{22} evolution. A general trend in the magnitude and shape evolution of the non-linear force-stress coupling is not discernable.

Fig. 9a–d show the Σ_{11} vs E_{11} and Σ_{22} vs E_{22} evolution for all LSX. LSB results in a stiffer Σ_{11} vs E_{11} and a more compliant Σ_{22} vs E_{22} elastic response in comparison to LSA. The hardening trend for both Σ_{11} vs E_{11} and Σ_{22} vs E_{22} during LSA and LSB is similar to that observed in Fig. 6. For LSA, reloading results in an increase in Σ_{11} of more than 100 MPa beyond its highest value during LP1, without any significant increase in E_{11}. For LSB, a similar increase in stress magnitude is observed for both Σ_{11} and Σ_{22}. For LSC, LSD and LSE, the Σ_{22} vs E_{22} curves follow an evolution trend that is similar to their corresponding F_2 vs E_{22} curves; the Σ_{11} vs E_{11} evolution is however very different from the corresponding F_1 vs E_{11} evolution. LSC and LSD, Σ_{11} vs E_{11} shows initial softening followed by hardening, whereas for LSE, Σ_{11} vs E_{11} shows a sharp elastic-plastic transition followed by an extended region of negative hardening ending in a low hardening regime. These peculiar responses are a combined consequence of the deformation history and the stress-force coupling in the cruciform geometry.

Fig. 9e–f show the VM stress Σ_{VM} vs accumulated total strain $\overline{E}$ (computed on the basis of the VM criterion) response for all LSX. A clear trend in the material response as a function of the reloading angle θ is evident. The material response becomes elastically stiffer as the reloading direction is changed away from nearly uniaxial tension along direction 1 towards equibiaxial tension, and it becomes

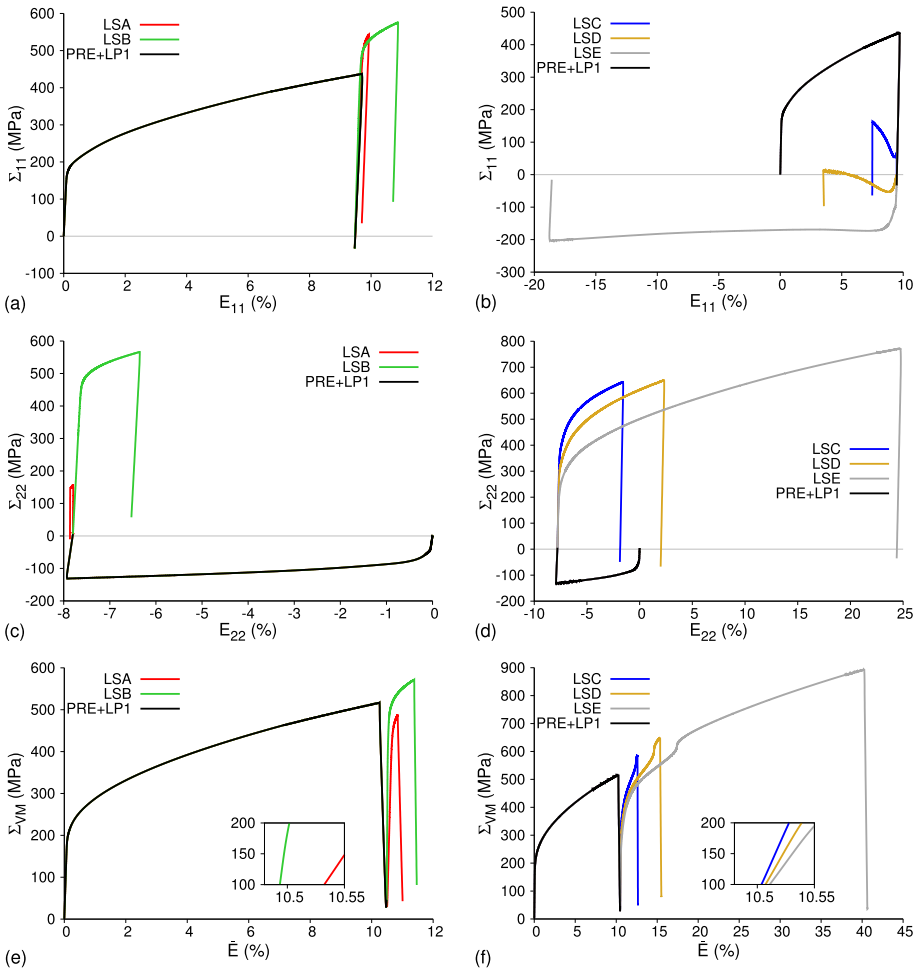

Fig. 9. Simulated (a, b) Σ_{11} vs E_{11}, (c, d) Σ_{22} vs E_{22}, and (e, f) Σ_{VM} vs $\bar{E}$ for (a, c, e) LSA and LSB, and (b, d, f) LSC, LSD and LSE. For clarity, PRE + LP1 for each LSX is highlighted in black. Insets of (e) and (f) highlight the differences in elastic stiffness during the second loading for all LSX.

more compliant as the reloading direction is changed away from equibiaxial tension towards uniaxial tension along 2. The apparent elastic stiffness for different LSX after PRE + LP1 is computed by fitting the curves using a straight line between Σ_{VM} = 100 and 150 MPa; these are found to be (in GPa) 273, 1370, 414, 322 and 252, respectively, for LSA, LSB, LSC, LSD and LSE. It is known that for a macroscopically elastically isotropic material, the Poisson effect results in a stiffer elastic response for an equibiaxial load in comparison to a uniaxial load (Van Petegem et al., 2016). The Poisson effect combined with the macroscopic and microscopic residual stresses results in the differences in the apparent elastic stiffness after PRE + LP1 for different LSX.

For a material that yields according to the VM yield criterion, the Σ_{11} vs E_{11} or the Σ_{22} vs E_{22} responses can be different but their Σ_{VM} vs $\bar{E}$ response follows the same elastic stiffness and hardening behavior. In this respect, the yield response of the reloaded 316L steel does not follow the VM yield criterion. Furthermore, the initial hardening response becomes harder as θ increases from 0° to 45°, and then softer as θ further increases from 45° to 90°.

The differences in the apparent elastic stiffness (in Fig. 9e and f) after the changes in load paths raises the question of what value of the effective elastic stiffness should be used to obtain the yield stress at 0.2% offset plastic strain from different LSX. Should it be the apparent elastic stiffness of individual LSX after the load path change or should it be the one for the initial un-deformed material? Bearing in mind the procedure to compute the 0.2% offset plastic strain, it should be the former approach. However, this results in significantly different effective elastic stiffness for different LSX. Nevertheless, following this method, one obtains the macroscopic yield stress (in MPa) as 480, 523, 384, 352 and 325, respectively, for LSA, LSB, LSC, LSD and LSE. The second load of LSB evidences a macroscopic yield stress that overshoots the highest Σ_{VM} attained during PRE + LP1, and vice versa for the remaining LSX. The extent of the elastic-plastic transition regime is different for each LSX. Furthermore, during the elastic-plastic regime for LSC, LSD and LSE loadings, a distinct non-linear kink is visible followed by a strong hardening response. These non-linear kinks arise from the coupling of gauge stresses due to the cruciform geometry which also causes the softening response and the plateau in the Σ_{11} vs E_{11} response for these loadings.

For a material that does not yield according to the VM criterion, the VM stress vs equivalent accumulated strain response may not

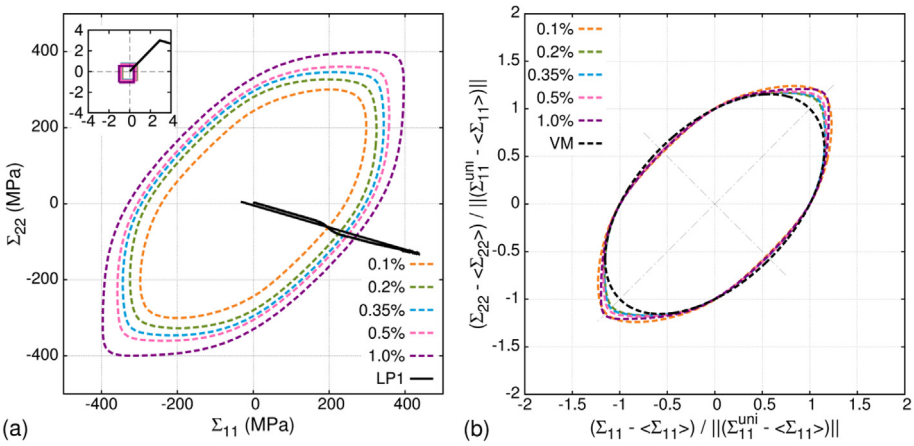

Fig. 10. (a) initial-PIPPS at E_0 = 0. 1%, 0.2%, 0.35%, 0.5%, and 1%, along with the Σ_{22} (MPa) vs Σ_{11} (MPa) evolution during PRE + LP1. Centroids for these PIPPS are shown in the inset in (a) and are colored according to the color of their corresponding PIPPS. (b) The shifted and normalized initial-PIPPS compared with the normalized VM yield surface. (For interpretation of the references to color in this figure legend, the reader is referred to the Web version of this article.)

be sufficient or appropriate to understand the biaxial load path change response of the material. This is mainly due to the differences in the apparent elastic stiffness which depends on θ. This further implies that the analysis of the biaxial response of the material needs to be performed in 2D space. In the next section, we analyze the stress and PIPPS evolution for each LSX in the 2D stress space to show that this is sufficient to understand the Bauschinger effect following a biaxial load path change.

4.3. PIPPS evolution

4.3.1. From initial microstructure

Fig. 10a shows the PIPPS at different E_0 from the initial microstructure and their centroids (mean position) in the 2D stress space; henceforth these shall be addressed as initial-PIPPS. At E_0 = 0.1%, the centroid is located at the zero-stress position. As E_0 increases, the centroids deviate very slightly away from the origin which is probably related to the limited number of strain probes (72) for PIPPS calculation. The centroid at zero stress position is a signature of a random texture without deformation history. Fig. 10b shows the initial-PIPPS whose centroids ($<\Sigma_{11}>$, $<\Sigma_{22}>$) have been shifted to the origin followed by a normalization of the shifted initial-PIPPS ($\Sigma_{11} - <\Sigma_{11}>$, $\Sigma_{22} - <\Sigma_{22}>$) with respect to the adjusted uniaxial tensile stress ($\Sigma_{11}^{uni} - <\Sigma_{11}>$). These are compared with the isotropic VM yield surface also shifted and normalized in a similar manner. All the initial-PIPPS are asymmetric about the lines passing through the origin and having slopes of tan 45° and tan 135°. Their shape differs from the VM yield surface with noticeable expansion along the equibiaxial direction; these may be fitted using anisotropic yield surfaces such as (Hill, 1948), among others. This agrees with the observations from Fig. 9.

Increasing E_0 results in an inhomogeneous expansion of the initial-PIPPS, however, a pattern for this expansion could not be deduced. The inhomogeneous expansion is the macroscopic manifestation of anisotropic slip activity at the granular level under different loading conditions and cannot be characterized with classical isotropic or kinematic hardening models. Phenomenological distortional hardening models (see (Manopulo et al., 2015) and references within) may be able to capture these inhomogeneous PIPPS shape changes but testing this is beyond the scope of present work.

Fig. 10a also shows the Σ_{22} vs Σ_{11} evolution during PRE + LP1 obtained from the VPSC-FE simulations; in the inset, the stress evolution during PRE loading is visible. During LP1 loading, the stress evolution is linear until Σ_{11} = 150MPa which marks the end of the macroscopic elastic regime. The slope of this curve is equal to − 0.29. The stresses begin to evolve non-linearly and the non-linearity becomes significantly pronounced in the macroscopic elastic-plastic transition regime. The slope decreases until an inflection point in the curve (located on the PIPPS at E_0 = 0.1%) and then increases to − 0.3 at the end of the elastic-plastic transition regime. These changes are associated with the rate of change in plastic strain with respect to the change in stress; a detailed explanation can be found in (Upadhyay et al., 2017b). Following the elastic-plastic transition, the stresses continue to evolve further into the 4th quadrant till the end of loading.

The residual stress components after LP1 are $\Sigma_{11} = -32.91$ MPa and $\Sigma_{22} = 5.49$ MPa. This residual state will significantly affect the subsequent mechanical response.

4.3.2. After PRE + LP1

Fig. 11a shows the PIPPS generated with the microstructure obtained after the PRE + LP1 sequences, henceforth named PIPPS-after-LP1. Also, the Σ_{22} vs Σ_{11} evolution during different LSX is shown; note that for clarity the PRE and LP1 sequences have been omitted. Fig. 11b shows the shifted and normalized PIPPS-after-LP1 using a procedure similar to Fig. 10b. At low E_0 values, the deformation history (residual stress, dislocation activity, etc.) from the first load and the elastic response after the load path change

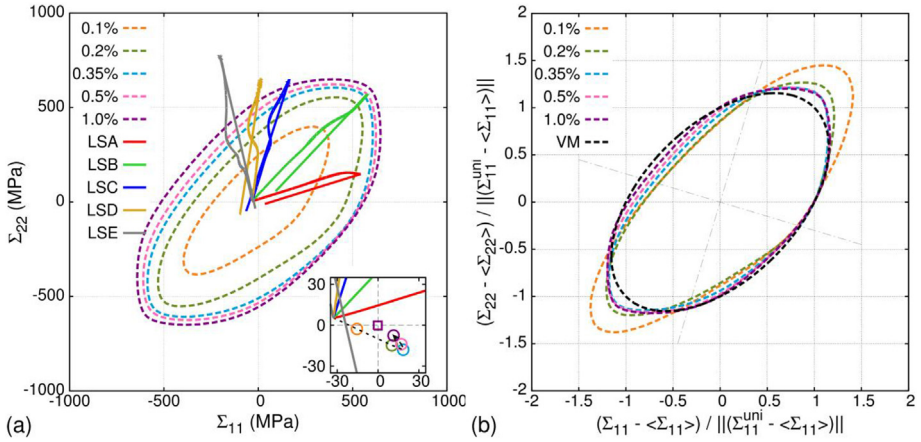

Fig. 11. (a) PIPPS-after-LP1 at E_0 = 0. 1%, 0.2%, 0.35%, 0.5%, and 1%, along with the Σ_{22} (MPa) vs Σ_{11} (MPa) evolution for all LSX. For clarity, the stress evolution during PRE + LP1 is omitted. The inset in figure (a) shows the centroids of the PIPPS-after-LP1. These are denoted using empty circles and colored according to the color of their corresponding PIPPS. The centroids of the PIPPS of the initial microstructure are also shown using the same convention as in Fig. 10a. The dotted-line arrow connects the centroids of the PIPPS-after-LP1 as a function of increasing E_0. (b) The shifted and normalized PIPPS-after-LP1 compared with the VM yield surface. The shifting and normalizing procedure is the same as for the initial-PIPPS shown in Fig. 10b. (For interpretation of the references to color in this figure legend, the reader is referred to the Web version of this article.)

significantly shift and distort the PIPPS-after-LP1. A distinct bulge along the direction of LP1 loading can be seen for the PIPPS-after-LP1 at E_0 = 0.1%, 0.2% and 0.35%. From E_0 = 0.35% to 1%, the bulge along the direction of loading decreases rapidly, and the shape of the PIPPS-after-LP1 approaches that of the VM yield surface and the initial-PIPPS at E_0 = 1%. This implies that the effect of deformation history on the PIPPS shape rapidly diminishes with increasing strain, irrespective of the reloading direction. As E_0 increases from 0.1% to 0.35%, the centroid of the PIPPS-after-LP1 tends to move away from the centroid of the initial-PIPPS. The opposite trend is observed as E_0 increases from 0.35% to 1%. The initial evolution of the centroid of PIPPS-after-LP1 away from the centroid of initial-PIPPS coincides with the significant distortions in the PIPPS-after-LP1. As these distortions being to diminish with increasing E_0, the centroid of PIPPS-after-LP1 tends towards the centroid of the initial-PIPPS. This implies that as deformation progresses, the PIPPS' shape evolution is decreasingly dependent on the deformation history from the first load and increasingly governed by the underlying texture evolution and its effect on dislocation activity. In contrast, the size of the PIPPS depends significantly on the deformation history.

The extent of the elastic regime and the yield response during reloading is highly dependent on the residual stress state and the shape of the PIPPS. During LP1 loading, even though the stress vector was in the 4th quadrant of the 2D stress space, significant PIPPS-after-LP1 (Fig. 11b) expansion is observed along the equibiaxial loading direction at low E_0 values; the explanation for this behavior is given in section 5. This implies that reloading from the residual stress state in the 2nd quadrant to equibiaxial tension (LSB) in the 1st quadrant will result in an extended macroscopic elastic regime. In contrast, reloading in the 2nd quadrant (LSD and LSE), or in its vicinity (LSC) will result in an earlier elastic-plastic transition. Furthermore, reloading at nearly 90° from the equibiaxial direction in the 2nd quadrant i.e. LSE, results in the earliest macroscopic elastic-plastic transition response. This conforms well with the observations in Fig. 9.

The Bauschinger effect is the change in yield strength due to internal stresses generated during deformation. Usually, it is studied for uniaxial loading, unloading, and reverse loading sequence in tension/compression/shear. A clear tension/compression asymmetry is observed along the horizontal axis in Fig. 11b but not along the vertical axis. Here we define the "biaxial Bauschinger effect" as the difference in the yield stress on a particular PIPPS along opposite directions of a single line that passes through the origin of the 2D stress space with any slope. The biaxial Bauschinger effect is clearly evident in PIPPS-after-LP1 with low E_0 values along some biaxial loading directions. This was not evident in the initial-PIPPS and is clearly a consequence of the deformation history. The biaxial Bauschinger effect diminishes with the diminishing shape distortions of the PIPPS-after-LP1. It is highly pronounced at E_0 = 0.1% and 0.2% along the line that passes through the origin and that is parallel to the direction of LP1 loading i.e. with a slope of − 0.3 (dot-dash grey line in Fig. 11b). It is the least pronounced along the line passing through the origin and with a slope of 3.33 (another dot-dash grey line in Fig. 11b). This line direction is nearly parallel to the stress vector during the second load of LSC. Interestingly, the biaxial Bauschinger effect diminishes significantly at E_0 = 1%.

Focusing on the stress response for each LSX, as the reloading stress ratio Σ_{22}/Σ_{11} changes further away from − 0.3 (the stress ratio at the end of LP1 loading), the non-linearity in the in-plane gauge stress evolution becomes more pronounced and complex. During LSA, at the end of the second load, there is a decrease in Σ_{22} while Σ_{11} is still increasing, which could not be deduced from Fig. 9. The second load during LSA ends close to the PIPPS-after-LP1 at E_0 = 0.2%. The final stress ratio during the LSA second load is Σ_{11}: Σ_{22} = 3.67: 1 which is significantly different from the applied load ratio i.e. F_1: F_2 = 2: 1. In fact, for all LSX except LSB the stress ratio at the end of second load is different from the applied force ratio highlighting the role of the cruciform geometry on the gauge response. During LSB, the Σ_{22} vs Σ_{11} evolution is nearly linear till the PIPPS-after-LP1 at E_0 = 0.1%. At the end of this loading, the stress state corresponds to the PIPPS-after-LP1 at $E_0 \approx$ 0.5%. The applied forces during the second loading of LSA and LSC follow the

ratios F_1: F_2 = 2: 1 and F_1: F_2 = 1: 2, respectively. However, from Fig. 7 it was seen that when $F_1^{LSA} = F_2^{LSC}$, the final accumulated strain increase is lower for LSA. This is now understood from the biaxial stress evolution and the PIPPS shape in Fig. 11. At the end of second loading for LSC, LSD and LSE, although F_2 = 60kN in each case, the stress and PIPPS shape evolutions give a clearer perspective on why LSE has the largest strain increments.

The unloading after each LSX results in significantly different residual stress states. LSA results in a residual stress state in the fourth quadrant of the 2D stress space whereas significantly large tensile residual stresses along both directions are obtained for LSB. Residual stresses after LSC, LSD and LSE are all in the third quadrant of the 2D stress space but have visible differences. A trend in the residual stresses could not be obtained based on the loading directions during LSX.

4.3.3. After all LSX

Fig. 12 shows the PIPPS after all LSX, referred as PIPPS-after-LSX. At E_0 = 1%, the PIPPS' size increases from LSA to LSE. Together with the strain evolution during second loading in Fig. 6, these results show that at larger E_0 the PIPPS size depends more on the accumulated strain than on the loading direction of the deformation history. At lower E_0 values, however, the loading direction of the deformation history plays an important role in determining the PIPPS size.

The centroids of the PIPPS-after-LSX follow the same trends as those observed for PIPPS-after-LP1; as E_0 increases, they tend towards the centroids of the initial-PIPPS. The centroid of PIPPS-after-LSB at E_0 = 0.1% is found to be the furthest away from the zero stress position whereas it is nearest for the PIPPS-after-LSE. This implies that the kinematic component of the macroscopic hardening at the beginning of the elastic-plastic transition regime depends significantly more on the direction of reloading with respect to the first load, than on the amount of accumulated strain during the whole loading sequence.

The shifted and normalized PIPPS-after-LSX were also analyzed; the figures are not shown here. Similar to the PIPPS-after-LP1 in Fig. 11, at low E_0 all PIPPS-after-LSX show pronounced shape distortions. At E_0 = 0.1%, LSB loading results in the highest elongation of the PIPPS-after-LSX; it is along the equibiaxial direction. This is a combined effect of LP1 loading and the reloading direction of LSB. Furthermore, the distortions in the direction of the second load are evident only for LSA and LSB but not for LSC, LSD and LSE. As E_0 increases, the distortions in the PIPPS-after-LSA and PIPPS-after-LSB rapidly subside. Interestingly, after LSC, LSD and LSE loadings, there is a delayed appearance of the distortions in the PIPPS; for instance, for PIPPS-after-LSC the bump is most pronounced at E_0 = 0.2% whereas for PIPPS-after-LSE this happens at E_0 = 0.35%. Furthermore, the biaxial Bauschinger effect in the direction of these distortions is the highest at E_0 = 0.2% for PIPPS-after-LSD and at E_0 = 0.35% for PIPPS-after-LSE. All PIPPS distortions significantly subside as E_0 increases from 0.35% to 1%. The rate at which these distortions subside with respect to increasing E_0 is fastest for LSA and slowest for LSE. These results indicate that higher amount of accumulated strain may result in delayed appearance of the full extent of the biaxial Bauschinger effect. Nevertheless, the biaxial Bauschinger effect can be observed in the initial stages of the elastic-plastic transition regime and it varies as a function of the proof strain E_0 (or offset plastic strain) depending on the deformation history.

Finally, the reduction in the biaxial Bauschinger effect with increasing E_0 coincides with the centroids of the PIPPS-after-LSX approaching the centroids of the initial-PIPPS. This indicates that the macroscopic kinematic hardening contribution significantly diminishes in early stages of biaxial reloading. These results are in agreement with studies performed on uniaxial load reversals. Furthermore, this indicates that a change in the biaxial Bauschinger effect corresponds to a change in the biaxial back-stresses in the material, and their rates of change should depend on the accumulated plastic strain during previous deformation and the reloading direction.

5. Discussion

In this work, the mechanical response of 316L steel cruciform samples subjected to biaxial load path changes was studied. The cruciform samples were subjected to the same uniaxial first load and then reloaded at different reloading angles θ in the range (0°, 90°]. The mechanical behavior was analyzed using a multi-scale modeling approach. To that end, the dislocation density based crystallographic-RGBV hardening law was implemented in the VPSC-FE model to, (1) capture the complex coupling between the applied forces and gauge stresses, and (2) capture the influence of deformation history and microstructural phenomena such as anisotropy, texture, dislocation activity, internal stresses, etc., on the macroscopic response. The model was successfully validated against these experiments and underlined the need to perform the analysis in 2D stress space since some aspects of the mechanical behavior cannot be explained from a uniaxial perspective. The stress and hardening behavior in the elastic and elastic-plastic transition regimes were found to highly depend on the uniaxial deformation history and the reloading angle.

The VPSC-FE model is however unable to account for grain level elastic strains that affect the yield behavior in the microplasticity regime; the VPSC model over-predicts the stress response in the early deformation stages. To overcome this problem, and to study the yield behavior and hardening response in the elastic-plastic transition regime, the EVP-FFT model was used to generate polycrystalline yield surfaces (PIPPS). The same crystallographic-RGBV hardening law was implemented in the EVP-FFT model and the same model parameters were used. VPSC-FE predicted gauge stresses were imposed as macroscopic boundary conditions to drive the EVP-FFT model. PIPPS before and after biaxial load path changes were then constructed using the EVP-FFT model. The shape distortions and centroid shifts of the PIPPS generated from the deformed microstructure helped to explain the differences in the elastic stiffness and hardening after different biaxial load path changes. The combined analysis of the VPSC-FE predicted cruciform gauge stress evolution along with the EVP-FFT predicted PIPPS evolution can explain the experimental biaxial load path change behavior at different reloading angles.

Recall that all the PIPPS are constructed at fixed E_0, which is a measure of total (elastic + plastic) strain and not the offset plastic

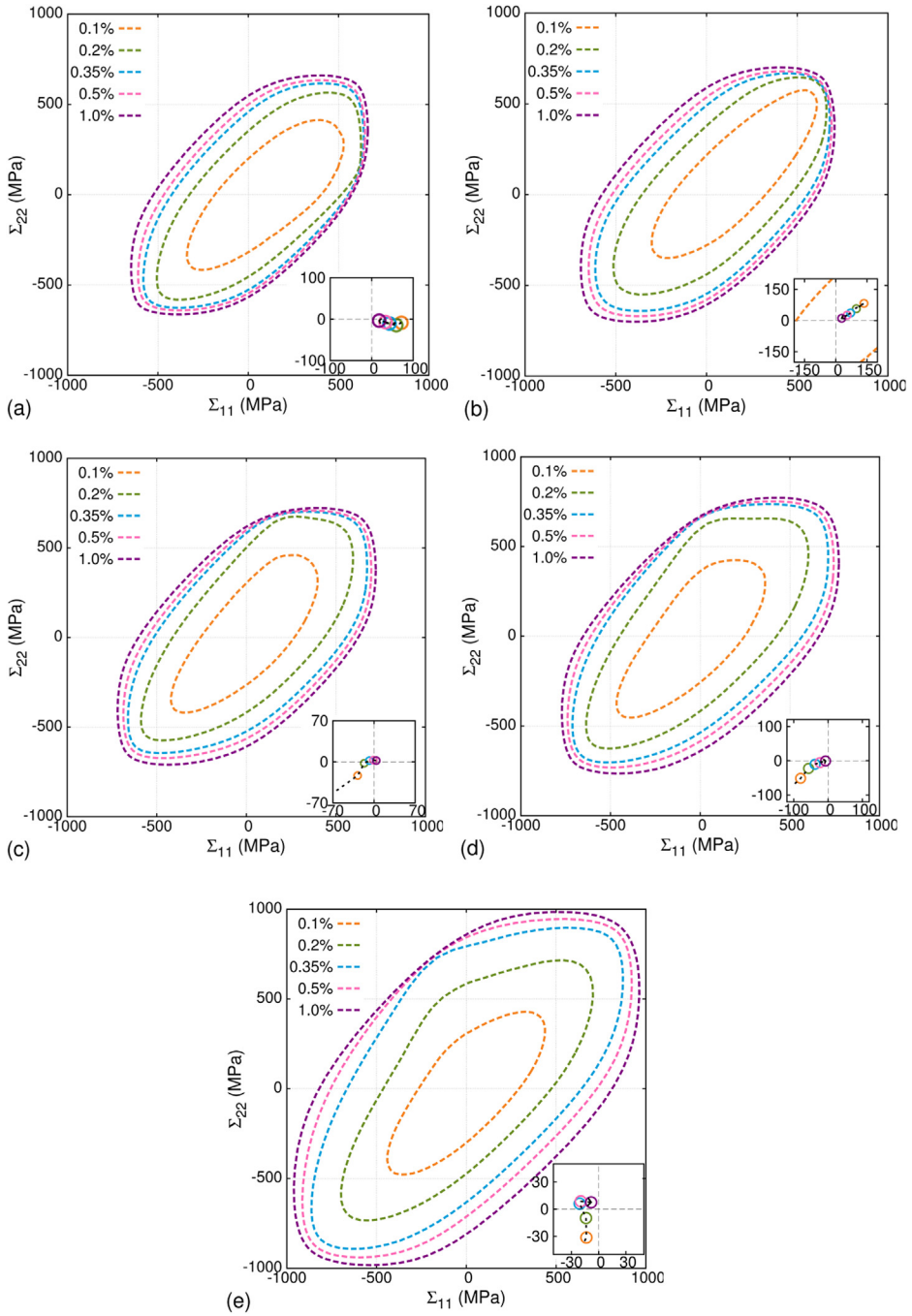

Fig. 12. PIPPS after (a) LSA, (b) LSB, (c) LSC, (d) LSD, and (e) LSE, at E_0 = 0. 1%, 0.2%, 0.35%, 0.5% and 1%. The insets in all these plots show the corresponding centroids for the PIPPS-after-LSX using empty circles. The centroids are colored according to the color of their corresponding PIPPS. Similar to Fig. 11a, the dotted-line arrow in each inset connects the centroids of the PIPPS-after-LSX as a function of increasing E_0. (For interpretation of the references to color in this figure legend, the reader is referred to the Web version of this article.)

strain. We have chosen to do this for the following reasons: (i) Computing the macroscopic yield stress from the VM stress vs the equivalent strain curves works well for a uniaxial loading case where the effective elastic stiffness is constant irrespective of a load path change. However, under biaxial load path changes, the effective elastic stiffness changes as a function of θ, as seen from Fig. 9e and f. Consequently, it is unclear which value of the elastic stiffness should be taken to extract the 0.2% offset plastic strain from the total strain. (ii) The EVP-FFT model requires imposing a macroscopic total strain rate. As seen in section 3.3, the norm of the imposed total strain rates is then used to compute the probe strain to generate the PIPPS. It is not trivial to extract an offset plastic strain (E_0^p) from this imposed probe total strain. One could envisage using the plastic work rate from equation (1) and approximate it as

$\dot{W}^p = \dot{E}_0^{vp} * f(\boldsymbol{\Sigma})$; where $f(\boldsymbol{\Sigma})$ is a function that returns a scalar value for $\boldsymbol{\Sigma}$. This can then be used to compute the $\dot{E}_0^{vp} = \dot{W}^p / f(\boldsymbol{\Sigma})$, which can be further used to compute E_0^p as $E_0^{p,t+\Delta t} = E_0^{p,t} + |\dot{E}_0^{vp,t+\Delta t}|\Delta t$. This procedure requires defining $f(\boldsymbol{\Sigma})$, which is open to interpretation. One could assume $f(\boldsymbol{\Sigma})$ to be equal to Σ_{VM} or any norm of the stress tensor, however, such an assumption would be arbitrary and result in an ambiguous interpretation of the PIPPS evolution. The disadvantages of using a total strain measure to construct the PIPPS are that, for a given E_0, (i) the ratio of the contribution of elastic and plastic strains changes as a function of θ and deformation history, and (ii) it is not possible to determine the magnitudes of these contributions. For instance, one can expect that the elastic strain contribution to initial-PIPPS at $E_0 = 0.35\%$ would be lower than its contribution to PIPPS-after-LSE at $E_0 = 0.35\%$, but one cannot compute E_0^p for either of these cases.

The Bauschinger effect was analyzed in the 2D stress space using the PIPPS. It was found to vary as a function of θ and the deformation history. It appeared and rapidly diminished along with the PIPPS distortions in the range $0.1\ \% \leq E_0 \leq 0.35\%$. Interestingly, for PIPPS-after-LP1 and all PIPPS-after-LSX, the largest PIPPS distortions appeared at different E_0 in this range. These results indicate that the full extent of the Bauschinger effect may not always manifest at 0.2% offset plastic strain.

For all biaxial load path changes, the Bauschinger effect manifests itself and rapidly diminishes in the early stages of the extended elastic-plastic transition regime. From TEM studies (Christodoulou et al., 1986; Fernandes et al., 1993; Hasegawa et al., 1975, 1986; Schmitt et al., 1991), it is known that the extended elastic-plastic transition regime during reloading is associated with dislocation annihilation and restructuring. Therefore, the dislocation slip activity after reloading may not be directly related to the presence/absence of the biaxial Bauschinger effect at larger strains. This implies that the biaxial Bauschinger effect is mainly dependent on the internal stress evolution and its macroscopic manifestation in the form of kinematic hardening. The extent of the Bauschinger effect may be quantified by studying lattice strain evolution from in-situ neutron diffraction studies. We have performed these experiments but their analysis is beyond the scope of present work and will be presented in a separate paper.

The shape of the PIPPS, and consequently the work-hardening rate, depend on the accumulated strain during deformation history and on the reloading angle. The origin of this has to be found in the character of the slip activity and the latent hardening effect at the single crystal level. To demonstrate this, the dislocation density evolution per slip system at the single crystal level is studied for the load sequence LSB (equibiaxial load path change), which shows elastically stiffest and plastically hardest reloading response amongst all LSX.

When a single crystal is subjected to an equibiaxial stress along two of its orthogonal crystallographic axes, 8 slip systems are activated (Upadhyay et al., 2016). Note that under a uniaxial compressive stress along the third crystallographic axis, the same 8 slip systems would be activated with equal RSS; this is because the deviatoric stress tensor is the same for equibiaxial tension (with component magnitude Σ) along two orthogonal directions and uniaxial compression (with magnitude $-\Sigma$) along the third orthogonal direction. To obtain a nearly equibiaxial stress state in a grain embedded in a polycrystalline RVE would require that the grain's crystallographic axes are aligned with those of the RVE as: $[100]_{grain} \| [100]_{RVE}$, $[010]_{grain} \| [010]_{RVE}$ and $[001]_{grain} \| [001]_{RVE}$. In the 100-grain RVE used in this work, none of the grains are aligned in such a manner. Therefore, a new grain with the aforementioned crystallographic relationship is introduced in the RVE.

VPSC-FE simulations are re-run using the new RVE for LSB loading. The total dislocation densities ρ_{tot}^s from equation (A3) for all slip systems belonging to this new grain are extracted from the gauge region, averaged over the mesh elements, and plotted as a function of Σ_{11} in Fig. 13. During LP1, four slip systems demonstrate high slip activity (ρ^3, ρ^6, ρ^9, ρ^{12}), another four show very low slip activity (ρ^2, ρ^5, ρ^8, ρ^{11}) and the remaining four are inactive (ρ^1, ρ^4, ρ^7, ρ^{10}). According to the equation set (A4), without any deformation history, the annihilation term for the reversible dislocation densities of the inactive slip systems is zero. Hence, there is no decrease in the ρ_{tot}^s of the inactive slip systems. Amongst the 4 active slip systems, there are appreciable differences in their ρ_{tot}^s. These differences arise from the anisotropic plastic interactions of the studied grain with the surrounding effective medium. During the

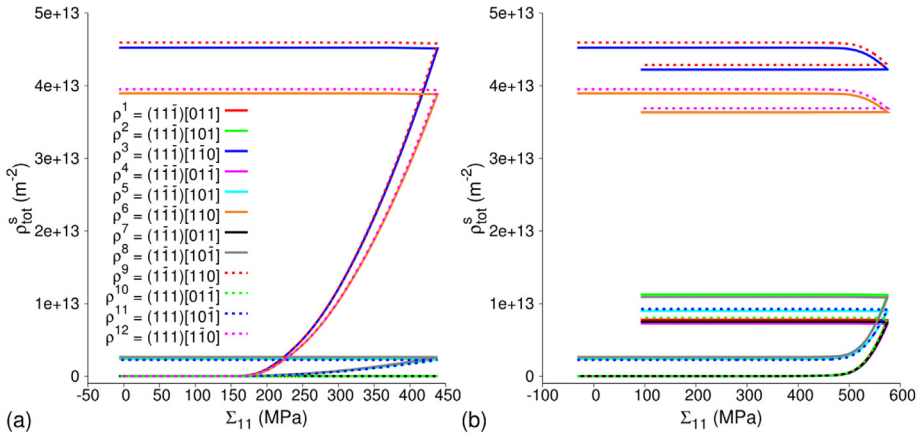

Fig. 13. Total dislocation density per slip system from a single grain in the RVE, and averaged over all integration points in the gauge region, ρ_{tot}^s (m^{-2}) vs Σ_{11} (MPa) during, (a) PRE + LP1, and (b) LP2 of LSB. The grain of interest is the one that has its crystallographic axes aligned to the RVE axes such that $[100]_{grain} \| [100]_{RVE}$, $[010]_{grain} \| [010]_{RVE}$ and $[001]_{grain} \| [001]_{RVE}$. The legend for both figures is shown in (a).

equibiaxial second load of LSB, a decrease in ρ^s_{tot} is observed for the 4 slip systems that exhibited the highest slip activity during LP1. This decrease indicates that (1) these slip systems are inactive during the second load and (2) the reversible dislocations generated on these slip systems during LP1 are annihilated according to the equation set (A4). Meanwhile, the remaining 8 slip systems are activated and their ρ^s_{tot} increases. There are some differences in the amount of increase in ρ^s_{tot} for these 8 slip systems which can be attributed to the anisotropic interaction of this grain with the effective medium. Furthermore, the overall increase in ρ^s_{tot} for these 8 slip systems is significantly lower in comparison to the ρ^s_{tot} increase during LP1 for the remaining 4 slips systems. This is because the CRSS of the former is higher during the second load due to latent hardening effects from dislocation activity of the latter slip systems during LP1. These changes in dislocation densities and CRSS affect the evolution of intra-granular stresses. Along with other microstructural phenomena, these determine the macroscopic response of the material.

The proposed modeling framework (VPSC-FE model with the dislocation density based hardening law) for reversible loading is a powerful tool to study multi-scale behavior during multi-axial load path changes. It allows studying material behavior at the microscale and thus goes beyond the reach of sophisticated macroscale plasticity models (Barlat et al., 2013; Raemy et al., 2017). Note that since the combined framework consists of three length scales, validating the approach at different lengths requires a multi-scale experimental data-set that contains the information on (a) sample geometry, (b) imposed boundary conditions, (c) distribution of gauge stresses and strains, (d) initial and final texture, (e) single crystal elastic and plastic properties, (f) distribution of intergranular stresses and strains, (g) evolution of intra-granular defect densities, among others. This would require combining multi-scale experimental approaches such as in-situ digital image correlation, in-situ neutron or synchrotron diffraction, and EBSD texture analysis of the un-deformed and deformed specimens. Bearing in mind that the aim was to study the macroscopic response, in this work the focus was on validating the combined model at the macroscopic scale while using only the essential information from lower length scales. Recall that the parameter fitting was performed only using the shear reverse-shear test which resulted in a non-unique set of parameters. These were sufficient to study the macroscopic behavior during cruciform load path changes. Identifying a unique set of parameters would require using data gathered from multiple experimental approaches that can access different regions of the stress space. In this aspect, multi-axial load path change tests such as the cruciform tests (with lower manufacturing tolerances), channel-die compression (Franciosi et al., 1987), tension-compression (Gonzalez et al., 2012) and tension-torsion (Takahashi et al., 1998) could be very useful. These tests could also be used to validate the model predictions at multiple length scales by also comparing information at lower length scales such as texture (Franciosi et al., 1987) and intergranular strains (Collins et al., 2015; Gonzalez et al., 2012; Van Petegem et al., 2016).

The multi-scale modeling framework also has its limitations. An important drawback in the VPSC model is that it cannot account for the elastic strains at the grain level and therefore can neither be directly used to predict intergranular strains nor to generate PIPPS at low strain values. To that end, SA polycrystalline EVP models that account for grain level elastic effects such as the EVPSC (Wang et al., 2010) and EVP-FFT approaches are needed. However, their computational costs are significantly higher than the VPSC-SA model, used in this work, making their implementation in an FE framework impractical. Meanwhile, the standalone EPSC-SA model was recently used to study the intergranular strain evolution during load path changes in Beryllium (Zecevic et al., 2015). More recently, the implementation of the EPSC model as the material model in ABAQUS FE (Zecevic et al., 2017) was used to study compression, cyclic loading and bending of different materials. The EPSC-FE model accounts for the grain level elastic effects and is computationally faster than the VPSC-FE approach, but cannot handle strain softening or strain rate effects. The VPSC-FE model, on the other hand, can handle strain softening and strain-rate effects. Recently, Knezevic and co-workers (Knezevic et al., 2016) proposed a modification to the constitutive equation in VPSC, called "*k*-modification" that eliminates the rate sensitivity introduced by the exponent n in equation (A6), and achieves a good trade-off between accuracy and speed. The k-modification approach was used by Zecevic et al. (2016) in the context of a VPSC-FE implementation. This approach was not used in the present work. Meanwhile, approaches such as the Taylor type crystal plasticity finite element (T-CPFE) model (Ardeljan et al., 2016) may be computationally faster than all the aforementioned methods but they only model a Taylor type grain interaction, thus losing accuracy. The choice of the multi-scale approach should depend on the intended application. In the present work, it was important to capture the load/strain rate effects that allow performing biaxial loading of cruciform samples at different force rates and displacement holds; this was well achieved using the VPSC-FE model.

A multi-scale mechanical model such as the one developed in this work is necessary to fully exploit the capabilities of cruciform testing. Furthermore, once the model has been appropriately validated, it can be used to study the mechanical behavior of complex engineering parts and processes for different material systems.

6. Conclusions

In this work, the mechanical response of 316L stainless steel cruciform samples subjected to different biaxial load path changes is studied. Five cruciform samples are subjected to the same uniaxial first load and unload, followed by in-plane reloading at $\theta = 27°$, 45°, 62°, 71° and 90° with respect to the uniaxial loading direction. The load path change response of these cruciform samples is interpreted using the VPSC-FE model. The VPSC-FE model is a three-level multi-scale model combining complex part geometry modeling at the macroscale, polycrystalline anisotropy and texture modeling at the meso-scale, and single crystal slip activity at the micro-scale. Polycrystalline yield surfaces (PIPPS) were generated using the EVP-FFT model and studied to understand the extent of Bauschinger effect in 2D stress space. The main conclusions of this experiment-modeling synergistic study are as follows:

1) The elastic stiffness of the material upon reloading depends on the first loading direction and the reloading angle θ. Following a uniaxial first load and unload, the elastic stiffness increases as θ increases from 0° to 45°, and decreases as θ increases from 45° to

90°; it is the highest during a 45° (equibiaxial) load path change.

2) The Bauschinger effect in 2D stress space (biaxial Bauschinger effect) depends on the reloading direction θ and the first loading direction, accumulated strain, and residual stresses. It appears in the early stages of the elastic-plastic transition regime and rapidly diminishes with increasing strain. The full extent of the Bauschinger effect may not manifest at 0.2% offset strain; the accumulated strain during the first loading sequence contributes in determining the reloading strain at which the full extent of the biaxial Bauschinger effect is realized. The origin of the biaxial Bauschinger effect may be found from the intergranular stress distribution.
3) The elastic-plastic transition regime can extend to proportionally larger strain values depending on the first loading direction and reloading angle θ. In the early stages, its evolution depends significantly on the deformation history and ,θ but rapidly changes to be dependent on the underlying texture and θ.
4) The work-hardening rates are strongly dependent on the first loading direction, accumulated strain during deformation history, and θ. They follow the same trends as a function of θ as the elastic stiffness. The origin of this is found at the single crystal level through the loading dependent heterogeneous slip activity and deformation history dependent latent hardening effects.

The cruciform geometry induces a non-linear coupling between the gauge stresses and applied forces. A multi-scale modeling approach, such as the one proposed in this work, is necessary to interpret cruciform experiment results. The combined experiment-modeling synergy has significant potential to help understand the multi-axial load path change behavior of engineering materials.

Acknowledgements

MVU and HVS acknowledge the financial support of the European Research Council (ERC) through the ERC advanced grant MULTIAX (339245). CNT acknowledges support from US Department of Energy, Office of Basic Energy Science, Division of Materials Science and Engineering, Project FWP 06SCPE401DOE-BES. The authors thank Dr. Jisik Choi and Prof. Frederic Barlat from POSTECH (Republic of Korea) for performing the shear reverse-shear tests whose results are used in this work.

Appendix

A1. A crystallographic dislocation density based hardening model for load path changes

The crystallographic-RGBV model (Kitayama et al., 2013; Wen et al., 2016) is used to predict the change in the critical resolved shear stress (CRSS) τ_c^s for each slip system s. The CRSS is decomposed into the contributions from dislocation accumulation/annihilation τ_d^s and back-stresses $\Delta\tau_B^s$ as follows:

$$\tau_c^s = \tau_d^s + \Delta\tau_B^s \tag{A1}$$

The dislocation accumulation/annihilation term is related to the dislocation density via the extended Taylor's law (Franciosi and Zaoui, 1982):

$$\tau_d^s = \tau_0^s + \mu b \sqrt{\sum_{s'} \alpha^{ss'} \rho^{s'}} \tag{A2}$$

where τ_0^s, μ, b, $\alpha^{ss'}$ and $\rho^{s'}$ are the initial CRSS, shear modulus, Burgers vector magnitude, interaction coefficient matrix between dislocations on slip system s and s', and the total dislocation density, respectively. The superscripts denote the slip systems s and s'. The diagonal and off-diagonal components of $\alpha^{ss'}$ correspond to self-hardening and latent hardening coefficients, respectively. The total dislocation density is decomposed into forward ρ_{for}^s and reversible dislocation densities ρ_{rev}^s. The forward dislocation density contributes to forest hardening whereas the reversible dislocation density accounts for those dislocations that recombine (annihilate) during a reversal of shear on the slip system s. A directional sense is given to the reversible dislocation densities by splitting each slip system into s^+ and s^- according to the positive or negative Burgers vector direction (arbitrarily assigned), respectively. Consequently, the total dislocation density on slip system s is:

$$\rho^s = \rho_{for}^s + \rho_{rev}^{s+} + \rho_{rev}^{s-} \tag{A3}$$

where ρ_{rev}^{s+} and ρ_{rev}^{s-} are the reversible dislocation densities on s^+ and s^-, respectively. The total dislocation density of all slip systems is defined as $\rho = \sum_s \rho^s$.

If the slip system s^+ is activated then the shear strain increment $d\gamma^{s^+} > 0$ and $d\gamma^{s^-} = 0$. The forward and reversible dislocation density increments are computed as:

$$\begin{aligned} d\rho_{for}^s &= (1-p)\frac{d\gamma^{s^+}}{b\Lambda} - f\rho_{for}^s d\Gamma \\ d\rho_{rev}^{s^+} &= p\frac{d\gamma^{s^+}}{b\Lambda} - f\rho^{s^+} d\Gamma \\ d\rho_{rev}^{s^-} &= -\frac{1}{b\Lambda}\left(\frac{\rho_{rev}^{s^-}}{\rho_0^s}\right)^m d\gamma^{s^+} \end{aligned} \tag{A4}$$

where $d\Gamma = \sum_s |d\gamma^s|$ is the total shear increment in one grain, b is the magnitude of the Burgers vector, ρ_0^s is the dislocation density on

slip system s at the beginning of a monotonic load sequence (it is equal to the total dislocation density on slip system s immediately after a load path change), f is a fitting parameter that determines the contribution to dislocation recovery, Λ is the dislocation mean-free path, and $0 < p < 1$ is a reversibility parameter that decreases as the dislocation density increases (Wen et al., 2016). When s^- is activated, then $d\gamma^{s^-} > 0$ and $d\gamma^{s^+} = 0$ and expressions similar to (A4) apply.

The back-stress contribution to CRSS on for slip system s, $\Delta\tau_B^s$, is related to the reversible dislocation densities as

$$\begin{aligned}\Delta\tau_B^s &= -\tau_d^s f_B^s \left(\frac{\rho_{rev}^{s^-}}{\rho^s}\right)^q \quad \text{if } d\gamma^+ > 0\\ \Delta\tau_B^s &= -\tau_d^s f_B^s \left(\frac{\rho_{rev}^{s^+}}{\rho^s}\right)^q \quad \text{if } d\gamma^- > 0\end{aligned} \tag{A5}$$

where f_B^s $(0 < f_B^s \leq 1)$ is a scaling factor, exponent q controls how fast the back-stress effect is nullified. Since the reversible dislocation densities increasingly recombine following a shear reversal, the contribution of back-stresses to CRSS proportionally decreases until it eventually vanishes. The numerical values of the model parameters for 316L stainless steel are reported in Table 1 in Section 3.1.

A2. Mean-field viscoplastic self-consistent polycrystal model

A2.1. VPSC-SA framework

In the mean-field VPSC framework (Lebensohn and Tomé, 1993), each grain is treated as an ellipsoidal viscoplastic inclusion embedded in a viscoplastic effective medium having the average mechanical properties and response of all the grains within the aggregate. Under the applied macroscopic strain rate or stress, the interaction between the effective medium with each grain is considered separately, causing a change in that grain's stress, strain, dislocation densities, crystallographic orientation, etc. These quantities are assumed to be uniform within the grain but deviate from the average values in the medium. At the level of individual grains, the deviatoric (superscript $'$) viscoplastic (superscript vp) strain rate tensor for a grain g, $\dot{\boldsymbol{\varepsilon}}^{vp,g}$, due to dislocation activity is defined using a power law relationship as:

$$\dot{\boldsymbol{\varepsilon}}^{vp,g} = \sum_s \boldsymbol{m}^s \dot{\gamma}^s = \dot{\gamma}^0 \sum_s \boldsymbol{m}^s \left(\frac{|\boldsymbol{m}^s : \boldsymbol{\sigma}^{g'}|}{\tau_c^s}\right)^n sgn(\boldsymbol{m}^s : \boldsymbol{\sigma}^{g'}) \tag{A6}$$

where $\boldsymbol{m}^s = \frac{1}{2}\left(\vec{\boldsymbol{b}}^s \otimes \vec{\boldsymbol{n}}^s + \vec{\boldsymbol{n}}^s \otimes \vec{\boldsymbol{b}}^s\right)$ is the Schmid tensor for slip system s; $\vec{\boldsymbol{b}}^s$ and $\vec{\boldsymbol{n}}^s$ are Burgers vector and normal vector, respectively, for the slip system s. $\boldsymbol{\sigma}^{g'}$ is the deviatoric stress tensor for grain g, $\dot{\gamma}^0$ is the reference shear rate, $\dot{\gamma}^s$ is the shear rate for slip system s, and n is the power law exponent. τ_c^s is defined as in equation (A1). A linearized constitutive relationship is used to correlate strain-rate and stress fields at the grain and aggregate levels as:

$$\begin{aligned}\dot{\boldsymbol{\varepsilon}}^{vp,g} &= \boldsymbol{M}^g : \boldsymbol{\sigma}^{g'} + \dot{\boldsymbol{\varepsilon}}_0^{p,g}\\ \dot{\mathbf{E}}^{\mathrm{vp}} &= \overline{\boldsymbol{M}} : \boldsymbol{\Sigma}' + \dot{\mathbf{E}}_0^{\mathrm{p}}\end{aligned} \tag{A7}$$

where $\boldsymbol{M}^g$ and $\overline{\boldsymbol{M}}$ are the 4th order local and macroscopic compliance tensors, respectively. $\dot{\boldsymbol{\varepsilon}}_0^{p,g}$ and $\dot{\mathbf{E}}_0^{\mathrm{p}}$ are the back-extrapolated plastic strain rates for the grain and the aggregate, respectively. The macroscopic quantities $\overline{\boldsymbol{M}}$ and $\dot{\mathbf{E}}_0^{p}$ are unknowns and are obtained by enforcing the conditions on the macroscopic deviatoric plastic strain rate and stress as $\dot{\mathbf{E}}^{\mathrm{vp}} = <\dot{\boldsymbol{\varepsilon}}^{vp,g}>$ and $\boldsymbol{\Sigma}' = <\boldsymbol{\sigma}^{g'}>$, respectively. The interaction between the mechanical fields of a grain and the aggregate are given as:

$$\dot{\boldsymbol{\varepsilon}}^{vp,g} - \dot{\mathbf{E}}^{\mathrm{vp}} = -\widetilde{\boldsymbol{M}} : (\boldsymbol{\sigma}^{g'} - \boldsymbol{\Sigma}') \tag{A8}$$

with

$$\widetilde{\boldsymbol{M}} = -n^{eff}(\boldsymbol{I} - \boldsymbol{S})^{-1} : \boldsymbol{S} : \overline{\boldsymbol{M}}^{secant} \tag{A9}$$

where n^{eff} describes the viscoplastic compliance of the inclusion-matrix (grain-aggregate) interactions: $n^{eff} = 0,\ 1$, and n, correspond to the Taylor, secant, and tangent cases, respectively (Lebensohn et al., 2007). In this work, $n^{eff} = 10$ is taken. $\boldsymbol{I}$ is the 4th order identity tensor. $\boldsymbol{S}$ is the 4th order Eshelby tensor for a given grain. $\overline{\boldsymbol{M}}^{secant}$ is the macroscopic viscoplastic compliance for the secant case.

A2.2. VPSC-FE interface

In the following, the VPSC-FE algorithm (Patra and Tomé, 2017; Segurado et al., 2012) implemented as a user material in ABAQUS is briefly recalled. Note here that the VPSC approach does not model the elastic response of the material. However, modeling the elastic response is necessary to create the VPSC-FE interface in ABAQUS. Therefore, the VPSC-FE interface is designed to account for macroscopic elastic strains obtained from the average macroscopic stresses and effective elastic stiffness of the material. Each integration or Gauss point in the FE mesh represents a polycrystalline microstructure. VPSC uses the local boundary conditions imposed by the VPSC-FE interface as homogeneous macroscopic conditions to compute the polycrystalline response at each integration point. The computed deformed state (stress and strain) at each integration point is then passed back to the FE code which solves for the global equilibrium in the FE mesh.

The VPSC-FE interface assumes an additive decomposition of the total strain increment into elastic and plastic parts i.e. $\Delta\mathbf{E} = \Delta\mathbf{E}^{e} + \Delta\mathbf{E}^{p}$. The elastic strain tensor $\Delta\mathbf{E}^{e}$ is computed from the stress increment $\Delta\boldsymbol{\Sigma}$ as $\Delta\mathbf{E}^{e} = \overline{\mathbf{C}}^{-1}$: $\Delta\boldsymbol{\Sigma}$, where $\overline{\mathbf{C}}$ is the self-consistent elastic stiffness tensor of the polycrystalline aggregate calculated from VPSC at the beginning of each increment. The plastic strain increment $\Delta\mathbf{E}^{p}$ is dependent on the stress state $\boldsymbol{\Sigma}$ (instead of stress increment) and internal state variables of the model (including the hardening law parameters). At each time increment, the FE code calls the VPSC-FE interface with an estimate of the stretch increment (total strain) $\Delta\mathbf{E}_{\mathrm{FE}}$, the rotation increment $\Delta\mathbf{R}_{\mathrm{FE}}$, and the time step increment, Δt. The VPSC-FE interface then uses the Newton-Raphson iterative procedure to solve for the stress increment $\Delta\boldsymbol{\Sigma}$ and consequently the corresponding stress state $\boldsymbol{\Sigma}$. The trial stress at time, $t + \Delta t$, is estimated as:

$$\boldsymbol{\Sigma}_{t+\Delta t} = \boldsymbol{\Sigma}_{t} + \Delta\boldsymbol{\Sigma} = \boldsymbol{\Sigma}_{t} + \overline{\mathbf{C}}\colon \Delta\mathbf{E}^{e} = \boldsymbol{\Sigma}_{t} + \overline{\mathbf{C}}\colon (\Delta\mathbf{E} - \Delta\mathbf{E}^{p}) \tag{A10}$$

where the subscript refers to the respective time increments. The stress state $\boldsymbol{\Sigma}_{t+\Delta t}$ is used as homogeneous macroscopic boundary condition to drive the VPSC model. VPSC computes the viscoplastic strain rate $\Delta\dot{\mathbf{E}}^{\mathrm{vp}}$. VPSC-FE interface then computes the residual between $\Delta\mathbf{E}$ and $\Delta\mathbf{E}_{\mathrm{FE}}$ as:

$$\boldsymbol{X}(\Delta\boldsymbol{\Sigma}) = \Delta\mathbf{E} - \Delta\mathbf{E}_{\mathrm{FE}} = \overline{\mathbf{C}}^{-1}\colon \Delta\boldsymbol{\Sigma} + \dot{\mathbf{E}}^{\mathrm{vp}}\Delta t - \Delta\mathbf{E}_{\mathrm{FE}} \tag{A11}$$

A scalar weighted convergence metric χ is used to achieve accelerated convergence.

$$\chi = \sqrt{\sum_{i}\sum_{j}\left(\frac{|\Delta E^{ij}_{\mathrm{FE}}|}{\max(|\Delta E^{ij}_{\mathrm{FE}}|)}X^{ij}\right)^{2}} \tag{A12}$$

where superscripts i and j denote the respective indices of the tensor quantities. If the convergence criteria is not satisfied for iteration k, then the trial stress increment for the $k + 1$ iteration is computed as,

$$(\Delta\boldsymbol{\Sigma})_{k+1} = (\Delta\boldsymbol{\Sigma})_{k} - \boldsymbol{J}^{-1}_{NR}((\Delta\boldsymbol{\Sigma})_{k})\colon \boldsymbol{X}((\Delta\boldsymbol{\Sigma})_{k}) \tag{A13}$$

where the Jacobian of the Newton-Raphson scheme is given as,

$$\boldsymbol{J}_{NR}(\Delta\boldsymbol{\Sigma}) = \frac{\partial\boldsymbol{X}(\Delta\boldsymbol{\Sigma})}{\partial(\Delta\boldsymbol{\Sigma})} = \overline{\mathbf{C}}^{-1} + \overline{\boldsymbol{M}}\Delta t \tag{A14}$$

VPSC computes all the macroscopic quantities in the coordinate system in which the texture of the material is prescribed. This needs to be rotated to the global coordinate system of the FE code. The VPSC-FE interface performs the necessary rotations via the tensor, $\mathbf{R} = \Delta\mathbf{R}_{\mathrm{FE}}\cdot\mathbf{R}_{\mathrm{t}}$ before passing them from the FE code onto VPSC (and vice versa); $\mathbf{R}_{t}$ is the total rotation at the end of time t.

A3. The full-field EVP-FFT model

The EVP-FFT model proposed in the work of (Lebensohn et al., 2012), is a full-field polycrystalline approach that consists of iteratively solving for a compatible total strain field (elastic + plastic strain). This model was developed based on the elastic FFT model for composites by (Moulinec and Suquet, 1994, 1998) and viscoplastic FFT model by (Lebensohn, 2001) using the augmented Lagrangian technique for faster convergence (Michel et al., 2000, 2001). This model accounts for the contributions of both elastic and plastic strains, as opposed to the VPSC approach that only accounts for the plastic strains. Furthermore, EVP-FFT requires prescribing the actual grain morphology and neighborhood, in contrast to the VPSC approach that assumes ellipsoidal grains embedded in an effective medium with average properties. In this work, the EVP-FFT model is used to compute polycrystalline iso-plastic-potential surfaces described in section 3.3.

In the EVP-FFT approach the polycrystalline microstructure is discretized into a grid of equi-spaced 3-dimensional voxels (or Fourier points). A grain in the polycrystalline domain can be defined using one or a collection of voxels adjacent to each other and having the same crystallographic orientation. The EVP-FFT algorithm involves solving the stress equilibrium, displacement continuity, and elastic and plastic constitutive relationships at each voxel. The constitutive behavior of an EVP material at each voxel is defined, under the infinitesimal strain approximation, as:

$$\boldsymbol{\sigma} = \boldsymbol{C}\colon \boldsymbol{\varepsilon}^{e} = \boldsymbol{C}\colon (\boldsymbol{\varepsilon} - \boldsymbol{\varepsilon}^{p}) \tag{A15}$$

where $\boldsymbol{\sigma}$, $\boldsymbol{C}$, $\boldsymbol{\varepsilon}^{e}$, $\boldsymbol{\varepsilon}^{p}$, and $\boldsymbol{\varepsilon}$ are the local Cauchy stress, elastic compliance, elastic strain, plastic strain and total strain tensors, respectively; the total strain additively decomposes into elastic and plastic strain components. The above equation is solved using an Euler-implicit time discretization scheme:

$$\boldsymbol{\sigma}^{t+\Delta t} = \boldsymbol{C}\colon (\boldsymbol{\varepsilon}^{t+\Delta t} - \boldsymbol{\varepsilon}^{p,t} - \dot{\boldsymbol{\varepsilon}}^{vp,t+\Delta t}(\boldsymbol{\sigma}^{t+\Delta t})\Delta t) \tag{A16}$$

where the superscript $t + \Delta t$and t denote the quantities at the current and previous time steps, respectively. The viscoplastic strain rate $\dot{\boldsymbol{\varepsilon}}^{vp}$ at each voxel is computed using equation (A6). The evolution of τ_{c}^{s} is modeled using equation (A1). For further details on the EVP-FFT algorithm, the interested reader is referred to the work of (Lebensohn et al., 2012).

References

Ardeljan, M., Beyerlein, I.J., McWilliams, B.A., Knezevic, M., 2016. Strain rate and temperature sensitive multi-level crystal plasticity model for large plastic deformation behavior: application to AZ31 magnesium alloy. Int. J. Plast. 83, 90–109. https://doi.org/10.1016/j.ijplas.2016.04.005.

Arul Kumar, M., Beyerlein, I.J., Tomé, C.N., 2017. A measure of plastic anisotropy for hexagonal close packed metals: application to alloying effects on the formability of Mg. J. Alloy. Comp. 695, 1488–1497. https://doi.org/10.1016/j.jallcom.2016.10.287.

Barlat, F., Gracio, J.J., Lee, M.-G., Rauch, E.F., Vincze, G., 2011. An alternative to kinematic hardening in classical plasticity. Int. J. Plast. 27, 1309–1327. https://doi.org/10.1016/j.ijplas.2011.03.003.

Barlat, F., Ha, J., Grácio, J.J., Lee, M.-G., Rauch, E.F., Vincze, G., 2013. Extension of homogeneous anisotropic hardening model to cross-loading with latent effects. Int. J. Plast., Microstructure-based Models of Plastic Deformation 46, 130–142. https://doi.org/10.1016/j.ijplas.2012.07.002.

Beyerlein, I.J., Tomé, C.N., 2008. A dislocation-based constitutive law for pure Zr including temperature effects. Int. J. Plast. 24, 867–895. https://doi.org/10.1016/j.ijplas.2007.07.017.

Beyerlein, I.J., Tomé, C.N., 2007. Modeling transients in the mechanical response of copper due to strain path changes. Int. J. Plast. 23, 640–664. https://doi.org/10.1016/j.ijplas.2006.08.001.

Bonnand, V., Chaboche, J.L., Gomez, P., Kanouté, P., Pacou, D., 2011. Investigation of multiaxial fatigue in the context of turboengine disc applications. Int. J. Fatigue. Multiaxial Fatigue Models 33, 1006–1016. https://doi.org/10.1016/j.ijfatigue.2010.12.018.

Borodachenkova, M., Wen, W., Barlat, F., Pereira, A., Grácio, J., 2015. Modeling of the mechanical behavior and texture evolution in Zn alloys during reverse shear loading. J. Mater. Process. Technol. 224, 143–148. https://doi.org/10.1016/j.jmatprotec.2015.04.021.

Brenner, R., Lebensohn, R.A., Castelnau, O., 2009. Elastic anisotropy and yield surface estimates of polycrystals. Int. J. Solid Struct. 46, 3018–3026. https://doi.org/10.1016/j.ijsolstr.2009.04.001.

Canova, G.R., Kocks, U.F., Tomé, C.N., Jonas, J.J., 1985. The yield surface of textured polycrystals. J. Mech. Phys. Solid. 33, 371–397. https://doi.org/10.1016/0022-5096(85)90035-3.

Choi, J.S., Lee, J.W., Kim, J.-H., Barlat, F., Lee, M.G., Kim, D., 2015. Measurement and modeling of simple shear deformation under load reversal: application to advanced high strength steels. Int. J. Mech. Sci. 98, 144–156. https://doi.org/10.1016/j.ijmecsci.2015.04.014.

Christodoulou, N., Woo, O.T., MacEwen, S.R., 1986. Effect of stress reversals on the work hardening behaviour of polycrystalline copper. Acta Metall. 34, 1553–1562. https://doi.org/10.1016/0001-6160(86)90100-8.

Cláudio, R.A., Reis, L., Freitas, M., 2014. Biaxial high-cycle fatigue life assessment of ductile aluminium cruciform specimens. Theor. Appl. Fract. Mech. 73, 82–90. Special Issue on Current models in multiaxial fatigue and fracture - in memory of Professor Ewald Macha. https://doi.org/10.1016/j.tafmec.2014.08.007.

Collins, D.M., Erinosho, T., Dunne, F.P.E., Todd, R.I., Connolley, T., Mostafavi, M., Kupfer, H., Wilkinson, A.J., 2017. A synchrotron X-ray diffraction study of non-proportional strain-path effects. Acta Mater. 124, 290–304. https://doi.org/10.1016/j.actamat.2016.11.011.

Collins, D.M., Mostafavi, M., Todd, R.I., Connolley, T., Wilkinson, A.J., 2015. A synchrotron X-ray diffraction study of in situ biaxial deformation. Acta Mater. 90, 46–58. https://doi.org/10.1016/j.actamat.2015.02.009.

Deng, N., Kuwabara, T., Korkolis, Y.P., 2015. Cruciform specimen design and verification for constitutive identification of anisotropic sheets. Exp. Mech. 55, 1005–1022. https://doi.org/10.1007/s11340-015-9999-y.

Feigenbaum, H.P., Dafalias, Y.F., 2014. Directional distortional hardening at large plastic deformations. Int. J. Solid Struct. 51, 3904–3918. https://doi.org/10.1016/j.ijsolstr.2014.07.011.

Fernandes, J.V., Gracio, J.J., Schmitt, J.H., Rauch, E.F., 1993. Development and persistence of microbands in copper deformed under complex strain paths. Scripta Metall. Mater. 28, 1335–1340. https://doi.org/10.1016/0956-716X(93)90478-B.

Franciosi, P., Berveiller, M., Zaoui, A., 1980. Latent hardening in copper and aluminium single crystals. Acta Metall. 28, 273–283. https://doi.org/10.1016/0001-6160(80)90162-5.

Franciosi, P., Stout, M.G., O'rourke, J., Erskine, B., Kocks, U.F., 1987. Channel die tests on Al and Cu polycrystals: study of the prestrain history effects on further large strain texture. Acta Metall. 35, 2115–2128. https://doi.org/10.1016/0001-6160(87)90040-X.

Franciosi, P., Zaoui, A., 1982. Multislip in f.c.c. crystals a theoretical approach compared with experimental data. Acta Metall. 30, 1627–1637. https://doi.org/10.1016/0001-6160(82)90184-5.

Franz, G., Abed-Meraim, F., Ben Zineb, T., Lemoine, X., Berveiller, M., 2009. Role of intragranular microstructure development in the macroscopic behavior of multiphase steels in the context of changing strain paths. Mater. Sci. Eng., A 517, 300–311. https://doi.org/10.1016/j.msea.2009.03.074.

Freund, M., Shutov, A.V., Ihlemann, J., 2012. Simulation of distortional hardening by generalizing a uniaxial model of finite strain viscoplasticity. Int. J. Plast. 36, 113–129. https://doi.org/10.1016/j.ijplas.2012.03.011.

Gonzalez, D., Kelleher, J.F., Quinta da Fonseca, J., Withers, P.J., 2012. Macro and intergranular stress responses of austenitic stainless steel to 90° strain path changes. Mater. Sci. Eng., A 546, 263–271. https://doi.org/10.1016/j.msea.2012.03.064.

Ha, J., Lee, J., Kim, J.H., Lee, M.-G., Barlat, F., 2017. Investigation of plastic strain rate under strain path changes in dual-phase steel using microstructure-based modeling. Int. J. Plast. 93, 89–111. Special Issue on Constitutive Descriptions of Plasticity atVarious Scales in memory of Prof. José J. Grácio. https://doi.org/10.1016/j.ijplas.2017.02.005.

Hasegawa, T., Yakou, T., Karashima, S., 1975. Deformation behaviour and dislocation structures upon stress reversal in polycrystalline aluminium. Mater. Sci. Eng. 20, 267–276. https://doi.org/10.1016/0025-5416(75)90159-7.

Hasegawa, T., Yakou, T., Kocks, U.F., 1986. Forward and reverse rearrangements of dislocations in tangled walls. Mater. Sci. Eng. 81, 189–199. Proceedings of the International Conference on Low Energy Dislocation Structures. https://doi.org/10.1016/0025-5416(86)90262-4.

Hill, R., 1948. A theory of the yielding and plastic flow of anisotropic metals. Proc. Roy. Soc. Lond. A 193, 281–297. https://doi.org/10.1098/rspa.1948.0045.

Hill, R., Hecker, S.S., Stout, M.G., 1994. An investigation of plastic flow and differential work hardening in orthotropic brass tubes under fluid pressure and axial load. Int. J. Solid Struct. 31, 2999–3021. https://doi.org/10.1016/0020-7683(94)90065-5.

Hill, R., Hutchinson, J.W., 1992. Differential hardening in sheet metal under biaxial loading: a theoretical framework. J. Appl. Mech. 59, S1–S9. https://doi.org/10.1115/1.2899489.

Hoferlin, E., Van Bael, A., Van Houtte, P., Steyaert, G., De Maré, C., 1998. Biaxial tests on cruciform specimens for the validation of crystallographic yield loci. J. Mater. Process. Technol. 80–81, 545–550. https://doi.org/10.1016/S0924-0136(98)00123-X.

Holmedal, B., Houtte, P.V., An, Y., 2008. A crystal plasticity model for strain-path changes in metals. Int. J. Plast. 24, 1360–1379. https://doi.org/10.1016/j.ijplas.2007.09.007.

Jeong, Y., Barlat, F., Tomé, C.N., Wen, W., 2017. A comparative study between micro- and macro-mechanical constitutive models developed for complex loading scenarios. Int. J. Plast. 93, 212–228. Special Issue on Constitutive Descriptions of Plasticity atVarious Scales in memory of Prof. José J. Grácio. https://doi.org/10.1016/j.ijplas.2016.07.015.

Kalidindi, S.R., Schoenfeld, S.E., 2000. On the prediction of yield surfaces by the crystal plasticity models for fcc polycrystals. Mater. Sci. Eng., A 293, 120–129. https://doi.org/10.1016/S0921-5093(00)01048-0.

Kitayama, K., Tomé, C.N., Rauch, E.F., Gracio, J.J., Barlat, F., 2013. A crystallographic dislocation model for describing hardening of polycrystals during strain path changes. Application to low carbon steels. Int. J. Plast. 46, 54–69. Microstructure-based Models of Plastic Deformation. https://doi.org/10.1016/j.ijplas.2012.09.004.

Knezevic, M., Beyerlein, I.J., Brown, D.W., Sisneros, T.A., Tomé, C.N., 2013a. A polycrystal plasticity model for predicting mechanical response and texture evolution during strain-path changes: application to beryllium. Int. J. Plast. 49, 185–198. https://doi.org/10.1016/j.ijplas.2013.03.008.

Knezevic, M., McCabe, R.J., Lebensohn, R.A., Tomé, C.N., Liu, C., Lovato, M.L., Mihaila, B., 2013b. Integration of self-consistent polycrystal plasticity with dislocation density based hardening laws within an implicit finite element framework: application to low-symmetry metals. J. Mech. Phys. Solid. 61, 2034–2046. https://doi.org/10.1016/j.jmps.2013.05.005.

Knezevic, M., Zecevic, M., Beyerlein, I.J., Lebensohn, R.A., 2016. A numerical procedure enabling accurate descriptions of strain rate-sensitive flow of polycrystals within crystal visco-plasticity theory. Comput. Meth. Appl. Mech. Eng. 308, 468–482. https://doi.org/10.1016/j.cma.2016.05.025.
Kuroda, M., Tvergaard, V., 1999. Use of abrupt strain path change for determining subsequent yield surface: illustrations of basic idea. Acta Mater. 47, 3879–3890. https://doi.org/10.1016/S1359-6454(99)00213-X.
Kuwabara, T., 2014. 1.06-Biaxial stress testing methods for sheet metals. In: Hashmi, S., Batalha, G.F., Tyne, C.J.V., Yilbas, B. (Eds.), Comprehensive Materials Processing. Elsevier, Oxford, pp. 95–111. https://doi.org/10.1016/B978-0-08-096532-1.00106-0.
Kuwabara, T., 2007. Advances in experiments on metal sheets and tubes in support of constitutive modeling and forming simulations. Int. J. Plast. 23, 385–419. NUMISHEET2005 Conference. https://doi.org/10.1016/j.ijplas.2006.06.003.
Kuwabara, T., Ikeda, S., Kuroda, K., 1998. Measurement and analysis of differential work hardening in cold-rolled steel sheet under biaxial tension. J. Mater. Process. Technol. 80–81, 517–523. https://doi.org/10.1016/S0924-0136(98)00155-1.
Kuwabara, T., Kuroda, M., Tvergaard, V., Nomura, K., 2000. Use of abrupt strain path change for determining subsequent yield surface: experimental study with metal sheets. Acta Mater. 48, 2071–2079. https://doi.org/10.1016/S1359-6454(00)00048-3.
Lebensohn, R.A., 2001. N-site modeling of a 3D viscoplastic polycrystal using fast fourier transform. Acta Mater. 49, 2723–2737. http://dx.doi.org/10.1016/S1359-6454(01)00172-0.
Lebensohn, R.A., Kanjarla, A.K., Eisenlohr, P., 2012. An elasto-viscoplastic formulation based on fast fourier transforms for the prediction of micromechanical fields in polycrystalline materials. Int. J. Plast. 32–33, 59–69. http://dx.doi.org/10.1016/j.ijplas.2011.12.005.
Lebensohn, R.A., Tomé, C.N., 1994. A self-consistent viscoplastic model: prediction of rolling textures of anisotropic polycrystals. Mater. Sci. Eng., A 175, 71–82. http://dx.doi.org/10.1016/0921-5093(94)91047-2.
Lebensohn, R.A., Tomé, C.N., 1993. A self-consistent anisotropic approach for the simulation of plastic deformation and texture development of polycrystals: application to zirconium alloys. Acta Metall. Mater. 41, 2611–2624. https://doi.org/10.1016/0956-7151(93)90130-K.
Lebensohn, R.A., Tomé, C.N., CastaÑeda, P.P., 2007. Self-consistent modelling of the mechanical behaviour of viscoplastic polycrystals incorporating intragranular field fluctuations. Philos. Mag. A 87, 4287–4322. https://doi.org/10.1080/14786430701432619.
Lee, J.-Y., Lee, M.-G., Barlat, F., Chung, K.-H., Kim, D.-J., 2016. Effect of nonlinear multi-axial elasticity and anisotropic plasticity on quasi-static dent properties of automotive steel sheets. Int. J. Solid Struct. 87, 254–266. https://doi.org/10.1016/j.ijsolstr.2016.01.020.
Liao, J., Sousa, J.A., Lopes, A.B., Xue, X., Barlat, F., Pereira, A.B., 2017. Mechanical, microstructural behaviour and modelling of dual phase steels under complex deformation paths. Int. J. Plast. 93, 269–290. Special Issue on Constitutive Descriptions of Plasticity atVarious Scales in memory of Prof. José J. Grácio. https://doi.org/10.1016/j.ijplas.2016.03.010.
Lowden, M. a. W., Hutchinson, W.B., 1975. Texture strengthening and strength differential in titanium-6Al-4V. Metall. Trans. A 6, 441. https://doi.org/10.1007/BF02658401.
Mánik, T., Holmedal, B., Hopperstad, O.S., 2015. Strain-path change induced transients in flow stress, work hardening and r-values in aluminum. Int. J. Plast. 69, 1–20. https://doi.org/10.1016/j.ijplas.2015.01.004.
Manopulo, N., Barlat, F., Hora, P., 2015. Isotropic to distortional hardening transition in metal plasticity. Int. J. Solid Struct. 56–57, 11–19. https://doi.org/10.1016/j.ijsolstr.2014.12.015.
Mecking, H., Kocks, U.F., 1981. Kinetics of flow and strain-hardening. Acta Metall. 29, 1865–1875. https://doi.org/10.1016/0001-6160(81)90112-7.
Merklein, M., Suttner, S., Brosius, A., 2014. Characterisation of kinematic hardening and yield surface evolution from uniaxial to biaxial tension with continuous strain path change. CIRP Ann. - Manuf. Technol. 63, 297–300. https://doi.org/10.1016/j.cirp.2014.03.039.
Michel, J.C., Moulinec, H., Suquet, P., 2001. A computational scheme for linear and non-linear composites with arbitrary phase contrast. Int. J. Numer. Meth. Eng. 52, 139–160. http://dx.doi.org/10.1002/nme.275.
Michel, J.C., Moulinec, H., Suquet, P., 2000. A computational method based on augmented Lagrangians and fast fourier transforms for composites with high contrast. Comput. Model. Eng. Sci. 1, 79–88. http://dx.doi.org/10.3970/cmes.2000.001.239.
Moulinec, H., Suquet, P., 1998. A numerical method for computing the overall response of nonlinear composites with complex microstructure. Comput. Meth. Appl. Mech. Eng. 157, 69–94. http://dx.doi.org/10.1016/S0045-7825(97)00218-1.
Moulinec, H., Suquet, P., 1994. A fast numerical method for computing the linear and nonlinear properties of composites. Comptes Rendus Académie Sci. Paris II 318, 1417–1423.
Patra, A., Tomé, C.N., 2017. Finite element simulation of gap opening between cladding tube and spacer grid in a fuel rod assembly using crystallographic models of irradiation growth and creep. Nucl. Eng. Des. 315, 155–169. https://doi.org/10.1016/j.nucengdes.2017.02.029.
Peeters, B., Seefeldt, M., Teodosiu, C., Kalidindi, S.R., Van Houtte, P., Aernoudt, E., 2001. Work-hardening/softening behaviour of b.c.c. polycrystals during changing strain paths: I. An integrated model based on substructure and texture evolution, and its prediction of the stress–strain behaviour of an IF steel during two-stage strain paths. Acta Mater. 49, 1607–1619. https://doi.org/10.1016/S1359-6454(01)00066-0.
Phillips, A., 1985. On the experimental foundation of the two surface model of plasticity and viscoplasticity. In: Sawczuk, A., Bianchi, G. (Eds.), Plasticity Today: Modelling, Methods and Applications. Elsevier, Amsterdam, pp. 221–234 Presented at the International Symposium on Current Trends and Results in Plasticity, Held at the International Centre for Mechanical Science, Udine, Italy, 27-30 June, 1983.
Phillips, A., Juh-Ling, T., 1972. The effect of loading path on the yield surface at elevated temperatures. Int. J. Solid Struct. 8, 463–474. https://doi.org/10.1016/0020-7683(72)90017-0.
Qin, J., Holmedal, B., Zhang, K., Hopperstad, O.S., 2017. Modeling strain-path changes in aluminum and steel. Int. J. Solid Struct. 117, 123–136. https://doi.org/10.1016/j.ijsolstr.2017.03.032.
Raemy, C., Manopulo, N., Hora, P., 2017. On the modelling of plastic anisotropy, asymmetry and directional hardening of commercially pure titanium: a planar Fourier series based approach. Int. J. Plast. 91, 182–204. https://doi.org/10.1016/j.ijplas.2017.02.010.
Rauch, E.F., Gracio, J.J., Barlat, F., 2007. Work-hardening model for polycrystalline metals under strain reversal at large strains. Acta Mater. 55, 2939–2948. https://doi.org/10.1016/j.actamat.2007.01.003.
Rauch, E.F., Gracio, J.J., Barlat, F., Vincze, G., 2011. Modelling the plastic behaviour of metals under complex loading conditions. Model. Simulat. Mater. Sci. Eng. 19, 035009. https://doi.org/10.1088/0965-0393/19/3/035009.
Savage, D.J., Beyerlein, I.J., Knezevic, M., 2017. Coupled texture and non-Schmid effects on yield surfaces of body-centered cubic polycrystals predicted by a crystal plasticity finite element approach. Int. J. Solid Struct. 109, 22–32. https://doi.org/10.1016/j.ijsolstr.2017.01.003.
Schmitt, J.H., Fernandes, J.V., Gracio, J.J., Vieira, M.F., Vieira, M.F., 1991. Plastic behaviour of copper sheets during sequential tension tests. Mater. Sci. Eng., A 147, 143–154. https://doi.org/10.1016/0921-5093(91)90840-J.
Segurado, J., Lebensohn, R.A., LLorca, J., Tomé, C.N., 2012. Multiscale modeling of plasticity based on embedding the viscoplastic self-consistent formulation in implicit finite elements. Int. J. Plast. 28, 124–140. https://doi.org/10.1016/j.ijplas.2011.07.002.
Shi, B., Peng, Y., Yang, C., Pan, F., Cheng, R., Peng, Q., 2017. Loading path dependent distortional hardening of Mg alloys: experimental investigation and constitutive modeling. Int. J. Plast. 90, 76–95. https://doi.org/10.1016/j.ijplas.2016.12.006.
Steglich, D., Jeong, Y., Andar, M.O., Kuwabara, T., 2012. Biaxial deformation behaviour of AZ31 magnesium alloy: crystal-plasticity-based prediction and experimental validation. Int. J. Solid Struct. 49, 3551–3561. New Challenges in Mechanics & Materials for Sheet Metal Forming. https://doi.org/10.1016/j.ijsolstr.2012.06.017.
Takahashi, H., Fujiwara, K., Nakagawa, T., 1998. Multiple-slip work-hardening model in crystals with application to torsion-tension behaviors of aluminium tubes. Int. J. Plast. 14, 489–509. https://doi.org/10.1016/S0749-6419(98)00004-7.
Takahashi, H., Shiono, I., 1991. Backlash model for large deformation behavior of aluminum under torsional cyclic loading. Int. J. Plast. 7, 199–217. https://doi.org/10.1016/0749-6419(91)90030-3.
Turner, P.A., Tomé, C.N., 1994. A study of residual stresses in Zircaloy-2 with rod texture. Acta Metall. Mater. 42, 4143–4153. https://doi.org/10.1016/0956-7151(94)90191-0.

Upadhyay, M.V., Capek, J., Petegem, S.V., Lebensohn, R.A., Swygenhoven, H.V., 2017a. Intergranular strain evolution during biaxial loading: a multiscale FE-FFT approach. JOM 69, 839–847. https://doi.org/10.1007/s11837-017-2299-5.

Upadhyay, M.V., Panzner, T., Petegem, S.V., Swygenhoven, H.V., 2017b. Stresses and strains in cruciform samples deformed in tension. Exp. Mech. 57, 905–920. https://doi.org/10.1007/s11340-017-0270-6.

Upadhyay, M.V., Van Petegem, S., Panzner, T., Lebensohn, R.A., Van Swygenhoven, H., 2016. Study of lattice strain evolution during biaxial deformation of stainless steel using a finite element and fast Fourier transform based multi-scale approach. Acta Mater. 118, 28–43. https://doi.org/10.1016/j.actamat.2016.07.028.

Van Petegem, S., Wagner, J., Panzner, T., Upadhyay, M.V., Trang, T.T.T., Van Swygenhoven, H., 2016. In-situ neutron diffraction during biaxial deformation. Acta Mater. 105, 404–416. https://doi.org/10.1016/j.actamat.2015.12.015.

Wang, H., Clausen, B., Tomé, C.N., Wu, P.D., 2013. Studying the effect of stress relaxation and creep on lattice strain evolution of stainless steel under tension. Acta Mater. 61, 1179–1188. https://doi.org/10.1016/j.actamat.2012.10.027.

Wang, H., Wu, P.D., Tomé, C.N., Huang, Y., 2010. A finite strain elastic–viscoplastic self-consistent model for polycrystalline materials. J. Mech. Phys. Solid. 58, 594–612. https://doi.org/10.1016/j.jmps.2010.01.004.

Wang, L., Huang, G., Quan, Q., Bassani, P., Mostaed, E., Vedani, M., Pan, F., 2014. The effect of twinning and detwinning on the mechanical property of AZ31 extruded magnesium alloy during strain-path changes. Mater. Des. 63, 177–184. https://doi.org/10.1016/j.matdes.2014.05.056.

Weiss, M., Kupke, A., Manach, P.Y., Galdos, L., Hodgson, P.D., 2015. On the Bauschinger effect in dual phase steel at high levels of strain. Mater. Sci. Eng., A 643, 127–136. https://doi.org/10.1016/j.msea.2015.07.037.

Wen, W., Borodachenkova, M., Tomé, C.N., Vincze, G., Rauch, E.F., Barlat, F., Grácio, J.J., 2016. Mechanical behavior of low carbon steel subjected to strain path changes: experiments and modeling. Acta Mater. 111, 305–314. https://doi.org/10.1016/j.actamat.2016.03.075.

Wen, W., Borodachenkova, M., Tomé, C.N., Vincze, G., Rauch, E.F., Barlat, F., Grácio, J.J., 2015. Mechanical behavior of Mg subjected to strain path changes: experiments and modeling. Int. J. Plast. 73, 171–183. Special Issue on Constitutive Modeling from Micro-Scale to Continuum in Honor of Prof. Frédéric Barlat. https://doi.org/10.1016/j.ijplas.2014.10.009.

Zecevic, M., Beyerlein, I.J., Knezevic, M., 2017. Coupling elasto-plastic self-consistent crystal plasticity and implicit finite elements: applications to compression, cyclic tension-compression, and bending to large strains. Int. J. Plast. 93, 187–211. Special Issue on Constitutive Descriptions of Plasticity atVarious Scales in memory of Prof. José J. Grácio. https://doi.org/10.1016/j.ijplas.2016.07.016.

Zecevic, M., Beyerlein, I.J., McCabe, R.J., McWilliams, B.A., Knezevic, M., 2016. Transitioning rate sensitivities across multiple length scales: microstructure-property relationships in the Taylor cylinder impact test on zirconium. Int. J. Plast. 84, 138–159. https://doi.org/10.1016/j.ijplas.2016.05.005.

Zecevic, M., Knezevic, M., Beyerlein, I.J., Tomé, C.N., 2015. An elasto-plastic self-consistent model with hardening based on dislocation density, twinning and de-twinning: application to strain path changes in HCP metals. Mater. Sci. Eng., A 638, 262–274. https://doi.org/10.1016/j.msea.2015.04.066.